One-Dimensional-Intergrowths in Two-Dimensional Zeolite Nanosheets and their Effect on Ultra-Selective Transport

Prashant Kumar^{1*}, Dae Woo Kim^{1,2,¶}, Neel Rangnekar^{1,¶}, Hao Xu^{4,¶} Evgenii O. Fetisov^{5,¶},

Supriya Ghosh¹, Han Zhang¹, Qiang Xiao⁶, Meera Shete¹, J. Ilja Siepmann^{1,5}, Traian Dumitrica⁴,

Benjamin McCool⁷, Michael Tsapatsis^{1,8,9}*, K. Andre Mkhoyan¹*

(Corresponding authors*: kumar141@umn.edu, tsapatsis@jhu.edu, mkhoyan@umn.edu)

(¶ indicates equal contribution)

¹ Department of Chemical Engineering and Materials Science, University of Minnesota, Minneapolis, MN

² Department of Chemical and Biomolecular Engineering, Korea Advanced Institute of Science and Technology, Daejeon 305-701, Republic of Korea

³ School of Chemical Engineering, Chonnam National University, Buk-gu, Gwangju, 61186 Republic of Korea

⁴ Department of Mechanical Engineering, University of Minnesota, Minneapolis, MN

⁵ Department of Chemistry and Chemical Theory Center, University of Minnesota, Minneapolis, MN

⁶ Key Laboratory of the Ministry of Education for Advanced Catalysis Materials, Institute of Physical Chemistry, Zhejiang Normal University, Jinhua, Zhejiang, China

 $^{^7}$ Separations and Process Chemistry, Corporate Strategic Research, Exxon Mobil Research and Engineering, Annandale, NJ 08801, USA

⁸ Department of Chemical and Biomolecular Engineering & Institute for NanoBioTechnology Johns Hopkins University, 3400 N. Charles Street, Baltimore, MD 21218 (USA)

⁹ Applied Physics Laboratory, Johns Hopkins University, 11100 Johns Hopkins Road, Laurel, MB 20723 (USA)

Zeolite MFI is a widely used catalyst and adsorbent, which also holds promise as a thin film membrane. The discovery of nm-thick 2-dimensional (2D) MFI nanosheets has enabled methods for thin film zeolite fabrication that open new horizons for membrane science and engineering. However, the crystal structure of 2D-MFI nanosheets and their relationship to separation performance remain clusive. Using transmission electron microscopy, we find that one- to few-unit-cells wide intergrowths of zeolite MEL exist within 2D-MFI. We identify the planar distribution of these 1-dimensional (1D) or near-1D-MEL domains, and show that a fraction of nanosheets have high (ca. 25% by volume) MEL content while the majority of nanosheets are MEL-free. Atomistic simulations show that commensurate knitting of 1D-MEL within 2D-MFI creates more rigid and highly selective pores compared to pristine MFI nanosheets, and permeation experiments show a separation factor of 60 using an industrially relevant (undiluted 1 bar xylene mixture) feed. Confined growth in graphite is shown to increase MEL content in MFI nanosheets. Our observation of these intergrowths suggests strategies for the development of ultra-selective zeolite membranes.

Commercially available zeolite membrane technologies are already enabling improved energy efficiency in industrial uses including dehydration and gas separations, and efforts directed towards expanding the range of their applications include hydrocarbon separations.¹ Certain mixtures of hydrocarbons, like xylene isomers, are difficult to separate and their production could become more efficient by the use of membranes that can operate with sufficiently high flux and selectivity at temperatures and pressures required for membrane-reactor configurations.² Membranes of the zeolite MFI, a widely-used industrial catalyst^{3–6} have been studied extensively for this application.^{7–9} However, membranes that can operate with sufficiently high flux and selectivity at industrial conditions are not yet available. Recent efforts towards MFI membranes

with improved performance are based on 2-dimensional (2D) MFI nanosheets. ^{10,11} However, the structure of 2D MFI nanosheets is not yet fully resolved and its connection to membrane flux and selectivity remains unknown.

MFI and MEL belong to the pentasil family of zeolites, which are frameworks with long chains of interconnecting five-membered Si-O tetrahedral units (pentasil chains)^{3,12}. Differences in connectivity of pentasil chains create a significantly different network of channels in MFI and MEL framework (Fig 1a-b). Along the crystallographic [010] direction (or b-direction), MFI exhibits inversion symmetry, while MEL shows mirror symmetry between neighboring pentasil chains¹³. These differences in pentasil chain connectivity result in sinusoidal channels along the [100] direction (or a-direction) and straight channels along the b-direction in MFI³, while in MEL the channels along both a- and b-direction are identical and straight¹². These differences in channel structures between MFI and MEL zeolites are detectable by transmission electron microscopy (TEM)¹³, which has been used extensively to reveal various types of MEL intergrowths in conventional MFI crystals^{14,15}. Here, we examine nanosheets prepared by exfoliation of multilamellar MFI^{10,11} after they have been subjected to a piranha solution treatment¹⁶. The piranha treatment removes the organic structure directing agent (SDA) used to synthesize the nanosheets and yields open-pore nanosheets with lateral area of ~ 200 nm x 200 nm and a thickness of 1.5 unit cells (3.2 nm, Fig 1c-d). As, up to now, no other structures have been detected in the nanosheets beyond MFI, they have been called 2D-MFI. However, in-plane x-ray diffraction (XRD) data obtained from oriented nanosheet monolayers (Fig 1e) revealed some inconsistencies in peak heights between a typical MFI pattern and the acquired pattern, suggesting the presence of MEL. A comparison of the intensity ratios of the (102) over (101) peak with simulated ratios for varying MEL content in MFI (Extended data Fig. 1, see methods) indicates that the nanosheets on

average contain 4.3% MEL by volume. The presence of this small quantity of MEL is not unexpected as it is known that MEL and MFI often co-exist¹⁵. In conventional crystals, it would have been very difficult to identify the MEL location. However, because nanosheets are of uniform 1.5-unit cell thickness, we hypothesized that TEM imaging of the MEL spatial distribution within MFI nanosheets could be possible.

Identification and Quantification of MEL in MFI Nanosheets

The use of TEM as a stand-alone technique or in combination with other methods (like XRD, atomic force microscopy (AFM), nuclear magnetic resonance (NMR) and infrared (IR) spectroscopy)^{17–19} to provide information about zeolite crystal structure and localized defects or features at the nanoscale is well established. However, beam-induced structural damage caused by radiolysis and knock-on mechanisms at low and high energy electrons²⁰ remain a challenge in achieving the highest possible resolution using TEM. To mitigate the electron beam damage during imaging of MFI nanosheets (Extended data Fig. 2a,b), we employed a high-energy electron-beam combined with low electron doses (see methods), and used an amorphous carbon support²¹ to minimize the sputtering of surface atoms via knock-on damage^{22–27}. Using aberration-corrected annular dark-field scanning transmission electron microscopy (ADF-STEM)^{28,29} we imaged the pentasil chain arrangement in the nanosheets (Extended data Fig. 2a). We found that the piranha treatment, which removes the organic SDA trapped within the MFI pores, facilitates the ADF-STEM examination of these nanosheets (our earlier efforts with SDA-containing nanosheets -not reported here- suffered from contamination that limited the achievable resolution). Further, we used post-acquisition digital image processing³⁰ (see methods for details) to increase the signal to noise ratio (SNR) of ADF-STEM images while preserving the features in the as-acquired image (Extended data Fig. 2c).

Identification of MFI and MEL across a single nanosheet was automated via cross-correlation of the simulated ADF-STEM images of unit cells (Extended data Fig. 3) with the ADF-STEM images of different regions (Extended data Figs. 4-6, see methods for details). While the majority of the nanosheets showed regions of pristine MFI framework (Fig. 2a), many regions showed semi-periodic arrangements of MFI and MEL domains (Fig. 2b,c). The MFI framework along the adirection is broken by insertions of near-single-unit-cell domains of MEL. Because the MEL insertions are extended only along the c-direction, we call them 1-D or near 1-D-MEL (Fig. 2b,c). Fast Fourier transforms (FFT) of images with such MEL insertions show elongated spots along the a*-direction as compared to a typical MFI spot pattern (Fig. 2a,b). This is an indication that presence of finite MFI domains in the a-direction has a fingerprint in reciprocal space of the crystal as elongation of spots along the a*-direction. The same method, when applied to high-resolution conventional bright-field (BF)-TEM images of nanosheets, produced similar outcome further confirming the observations (Extended Data Fig. 7, see methods for details). This observation prompted an analysis of the reciprocal space through electron diffraction patterns.

Selected area electron diffraction (SAED) patterns of nanosheets were acquired and analyzed. The majority of the nanosheets (ca. 55%) showed a typical [010] MFI zone axis pattern (Fig. 3a), indicating that the bulk of the sample is MFI-type. However, many nanosheets showed elongation (or broadening) of spots (Fig. 3b) with h+l=odd indices (102, 104, 203, etc.). Through structure factor calculations and SAED pattern simulations (Extended data Figs. 8 and 9a-c, see methods for details) of various distribution patterns for MFI and MEL within a nanosheet, it is confirmed that spots with h+l=odd indices are broadened due to the presence of finite domains of MFI trapped between MEL layers, along the **a**-direction. Broadened (102) as well as (101) spots were analyzed by fitting 2D-Gaussian functions (Fig 3c,d). The volume under the Gaussian fit for the

(102) peak (peak intensity, I_{102}) is a measure of MEL content and the full-width-at-half-maximum (peak broadening, $FWHM_{102}$) is a measure of the MFI domain width. Using calibration curves generated from simulations for I_{102}/I_{101} vs % MEL and $FWHM_{102}/FWHM_{101}$ (R) vs MFI domain width (d) (Extended data Fig. 9d, e, see methods), we found, upon analysis of SAED patterns from 50 MEL-containing nanosheets (Extended data Fig. 10), that the average volumetric MEL content was 25% with $\langle d \rangle_{ave} = 3$ unit cells (u.c., Fig. 3e,f). The calculated MEL content and MFI domain width are consistent with the MEL intergrowths being 1D-MEL insertions.

While XRD data gave an estimate that the overall MEL content in nanosheets is 4.3 % (Fig. 1), the TEM investigations revealed that the majority of individual nanosheets (ca. 55% of nanosheets) are MFI-type, and only a smaller fraction contains MEL. However, those that do contain MEL (ca. 45% of nanosheets) have a high MEL concentration (ca. 25%). Such nanosheets showed an average MFI-MEL heterostructure with repeating long chains of 1 u.c. MEL (1D-MEL), followed by 2-4 u.c. wide MFI domains. The TEM observations indicate up to 11% MEL content, which is in reasonable agreement with the overall, 4.3% MEL, content suggested by the in-plane XRD analysis.

The highly non-uniform MEL distribution (high MEL content in small fraction of nanosheets) and their 1D type are intriguing and unexpected findings. They underscore the power of TEM imaging to reveal single-unit-cell features that cannot be determined otherwise. Although MEL is known to intergrow with MFI, the presence of 1D-MEL intergrowths in 2D-nanosheets has not been observed before.

The interconnection of the 1D-MEL insertions within MFI should result in the creation of an interface, which is expected to deviate from the MFI framework. However, determining such deviations, if any, is beyond the resolution of our TEM imaging. Next, we attempt, using

simulations, to assess the implications of the knitting of 2D-MFI with 1D-MEL on the mechanical and molecular sieving properties of nanosheets and discuss consequences for nanosheet-based membrane performance.

Role of Intergrowth in Pore Deformation under Strain

Mechanical properties of MFI nanosheets with single-unit-cell MEL domains were examined using atomistic calculations. To study the impact of MEL content, nanosheet heterostructure models were created by inserting 1D MEL chains into MFI supercells with various sizes along the a-direction (Fig. 4a,b). The MFI-MEL coherent interfaces located in the (b, c) plane comprise fully connected Si-O-Si bonds (Supplementary Fig. 1). Due to the large number of atoms in these heterostructures, calculations were carried out with a computationally efficient classical ReaxFF potential.³¹ (Supplementary Fig. 2a,b). Simulations identified features of pores that are potentially beneficial for separation applications. First, it was observed that the elliptical MFI pores are particularly amenable to becoming more elliptical under compressive strains applied along the adirection (Supplementary Fig. 2c-f). With a Young's modulus (E) of 54 GPa, pure MFI is least stiff along the most sensitive a-direction (Table S1). On the contrary, MEL is stiffest along the adirection, and its computed E is substantially (about 20%) larger than that of MFI. Therefore, the heterostructure calculations of Fig. 4c indicate that incorporation of MEL brings an increase in the overall E along the a-direction, which should be beneficial for making the MFI pores less susceptible to deviations in circularity. Fig. 4c also shows that the Young's moduli along a and cdirections become equal for nanosheets with MEL-content between 20 and 33%, suggesting that the nanosheets in this range adopt isotropic in-plane mechanical properties. Second, the calculations reveal that the MEL pores preserve their size and shape, even when relatively large compressive strains (up to 5%) are applied along the a- and c- directions (Supplementary Fig. 2gh). Third, the calculations show that the MFI-MEL interfaces can introduce strain, and thus affect the original MFI pores. These interfacial pores respond to compressive strains in the same manner as the pristine MFI ones (Supplementary Fig. 2g-h), but they are smaller than their pristine MFI counterparts by ~ 0.2 Å in average diameter under no strain. Such small differences in pore sizes are difficult, if not impossible, to detect by TEM imaging. However, due to the reduced size of interface pores and increased stiffness of MEL as compared to MFI, their role in permeation performance of close-fitting molecules could be significant.

Role of Intergrowths in Membrane Performance

Among the possible uses of MFI membranes, the separation of xylene isomers is of both industrial interest and fundamental significance and remains a most challenging one due to the close fit of these aromatic molecules in MFI pores. Here, we assess the role of MEL intergrowths for p-xylene (kinetic diameter of 5.8 Å) over o-xylene (kinetic diameter of 6.8 Å) shape- and size-selectivity along the **b**-direction (thin dimension) of the nanosheets. Using first principles molecular dynamics simulations, the free-energy barriers for p-xylene and o-xylene diffusion were estimated (see methods for details, Supplementary Fig. 3a,b). It was observed that p-xylene and o-xylene molecules create significant structural distortions when passing through MFI and MEL pores (Supplementary Fig. 3c,d). Since MFI is more flexible as compared to MEL, it allows the easier passage of both p- and o-xylene molecules compared to MEL (smaller difference between energy barriers for MFI than MEL), which is much more resistive to the flow of o-xylene. Therefore, the MEL pore is more selective to p-xylene as compared to an MFI pore, while the interfacial MFItype pore behaves as an intermediate of both. Based on these diffusivity data, the p-/o-xylene selectivity enhancement for MFI-MEL heterostructures with different MFI and MEL fractions can be estimated (Fig. 4e, Supplementary Fig. 4 a,b). For example, nanosheets with 20%, 27% or 33 %

MEL content (α_{MEL} = 0.2, 0.27, 0.33), which is distributed as 1D-MEL insertions interrupting the continuity of 2D-MFI along the **a**-direction, exhibit a 1.4, 1.9, or 14-fold improvement in selectivity, respectively, as compared to a pristine MFI nanosheet (Table S2). The improvement in selectivity is mostly due to a drastic reduction of o-xylene diffusivity as MEL content increases, while p-xylene diffusivity is less affected by the MEL content (Fig. 4d). This means that a single MFI-MEL nanosheet membrane with the current level of 25% 1-D MEL content will exhibit similar p-xylene flux, but 1.7 times the selectivity of a pure MFI nanosheet membrane. According to this simple nanosheet model, an increase to 33% 1D-MEL content, by eliminating pure MFI domains (Supplementary Fig. 4b), would mark a transition to a remarkably (14-fold) improved selectivity.

Zeolite nanosheet-based membranes cannot yet be made as single nanosheets, but they consist of nanosheets arranged on top of each other as multilayers (typical thicknesses start from 10-nanosheet multilayers) with random in-plane orientation, which are then intergrown using various secondary growth methods^{11,32}. Membrane performance depends not only on transport through the original nanosheets but also through non zeolitic defects (gaps between nanosheets), newly intergrown sections (formed by epitaxial growth on nanosheets), and pore constrictions/blockages created during membrane synthesis. Moreover, strain induced from secondary growth, calcination (to remove the SDA) and hydrocarbon adsorption (during operation) further complicates the connection between membrane microstructure and separation performance, which remains an unsolved problem. Therefore, it is not possible to precisely determine the effect that the MEL-containing nanosheets, discovered herein, have on the membrane performance. However, an upper bound estimation can be attempted based on an idealized model of nanosheet-based membranes, which assumes that nanosheets are epitaxially registered on top of each other as multilayers with

typical thicknesses of these multilayers starting from a stack of 10-nanosheets (see Supplementary Fig. 4c and methods for details). As shown in Table S3, according to this idealized model, for nanosheets with a total MEL content of 4.3% (see Supplementary Fig. 4d), when the MEL is distributed as 1D-MEL in a fraction (x=0.13) of nanosheets, with the MEL-containing nanosheets having 27% MEL by volume ($\alpha_{MEL}=0.27$), a ~1.3-fold increase in selectivity can be achieved. For the same total MEL content (4.3%), if the MEL-containing nanosheets have 33% MEL content ($\alpha_{MEL}=0.33$), a 5.5-fold increase in selectivity is obtained. This estimation suggests that even at the current low levels, the MEL content in the reported nanosheet-based membranes can be a significant contributor to their experimentally established selectivity (providing a 1.3-5.5-fold enhancement compared to MEL-free nanosheets). Further performance improvements with more than 10-fold selectivity enhancements are possible, if the 33%-1D-MEL-containing nanosheet fraction can be increased further (Fig 4f, $\alpha_{MEL}=0.33$).

In agreement with the performance anticipated by the models described above, membranes made from MEL-containing exfoliated nanosheets using gel-free secondary growth exhibit highly paraxylene selective behavior with undetected ortho-xylene in the permeate (mixture separation factor > 1000) under dilute conditions (ca. para-xylene partial pressure of ca. 500Pa). The ultimate test for para-xylene selective zeolite membranes is their performance using undiluted hydrocarbon feeds as would be encountered in industrial use (e.g., in xylene isomerization membrane reactors). However, rarely zeolite membranes exhibit selectivity at conditions approaching undiluted xylene feeds^{8,33}. Hedlund and co-workers⁸ reported para-xylene/meta-xylene mixture separation factor of 13 at 400°C using a hydrocarbon feed diluted with hydrogen (para-xylene, meta-xylene, ethylbenzene, 1,3,5-trimethyl-benzene, hydrogen partial pressures of 25, 65, 5, 100 kPa, respectively). At comparable conditions (275-300°C with undiluted feed of para-xylene, ortho-

xylene, 1,3,5-trimethyl-benzene with partial pressures of 47.5, 47.5, 5KPa, respectively) our membranes show a 4.6-fold increase in mixture separation factor (Table 1). At higher pressures the separation factor dropped to 19.3 but still remained nearly four times higher than the corresponding one for MFI membranes, which exhibit mixture separation factor of 5. Although a definite proof cannot be provided, this selectivity improvement can be attributed to the improved rigidity and selectivity imparted to the nanosheets by the presence of 1-D MEL domains.

Of course, synthesis of pure MEL nanosheets is highly desirable. However, due to the tetragonal symmetry of MEL, synthesis of pure MEL nanosheets is expected to be very challenging if not impossible. A recent study showed that a product highly enriched in MEL can be prepared by manipulating steric hindrance and crowding of silicate species near modified SDAs under conditions of low SDA/SiO₂ ratio^{34,35}. However, the obtained product is in the form of needle-like crystals, not appropriate for membrane formation. Our alternative strategy to affect SDA-silicate interactions without replacing the standard SDA for multilamellar MFI (C₂₂-6-6Br₂), is to perform synthesis in the presence of an inert lamellar material. In the presence of graphite, we can obtain high-MEL-content, albeit thicker (10-20 nm), nanosheets (Supplementary Fig. 5-7) instead of multilamellar MFI. 64% of nanosheets (83 of 129 examined) synthesized in graphitic confinement contain up to 55% MEL, giving an average MEL content of 35% in the examined batch. We tentatively attribute this outcome to the confining effect of graphite nanosheets and to the reduced availability of C₂₂-6-6Br₂ SDA during synthesis due to its adsorption on graphite. These high-MELcontent nanosheets provide a new direction for systematic manipulation of permeation properties in zeolite membranes.

References

- 1. Rangnekar, N., Mittal, N., Elyassi, B., Caro, J. & Tsapatsis, M. Chem Soc Rev Zeolite membranes a review and comparison with MOFs. *Chem. Soc. Rev.* 44, 7128–7154 (2015).
- Daramola, M. O., Aransiola, E. F. & Ojumu, T. V. Potential applications of zeolite membranes in reaction coupling separation processes. *Materials (Basel)*. 5, 2101–2136 (2012).
- 3. Kokotailo, G., Lawton, S. & Olson, D. Structure of synthetic zeolite ZSM-5. *Nature* **272**, 437–438 (1978).
- 4. Flanigen, E. M. *et al.* Silicalite, a new hydrophobic crystalline silica molecular sieve. *Nature* **271**, 512–516 (1978).
- 5. Degnan, T. F., Chitnis, G. K. & Schipper, P. H. History of ZSM-5 fluid catalytic cracking additive development at Mobil. *Microporous Mesoporous Mater.* **35–36**, 245–252 (2000).
- Clough, M. et al. Nanoporous materials forge a path forward to enable sustainable growth:
 Technology advancements in fluid catalytic cracking. Microporous Mesoporous Mater.
 254, 45–58 (2017).
- 7. Lai, Z. *et al.* Microstructural optimization of a zeolite membrane for organic vapor separation. *Science* (80-.). **300**, 456–460 (2003).
- 8. Hedlund, J. et al. High-flux MFI membranes. *Microporous Mesoporous Mater.* **52**, 179–189 (2002).
- 9. Jeon, M. Y. *et al.* Ultra-selective high-flux membranes from directly synthesized zeolite nanosheets. *Nature* **543**, 690 (2017).
- 10. Choi, M. *et al.* Stable single-unit-cell nanosheets of zeolite MFI as active and long-lived catalysts. *Nature* **461**, 246–249 (2009).

- 11. Varoon, K. *et al.* Dispersible exfoliated zeolite nanosheets and their application as a selective membrane. *Science* **334**, 72–75 (2011).
- 12. Kokotailo, G., Chu, P. & Lawton, S. Synthesis and structure of synthetic zeolite ZSM-11.

 Nature 275, 119–120 (1978).
- 13. Ohsuna, T. & Terasaki, O. Electron Microscopic Study of Intergrowth of MFI and MEL: Crystal Faults in B-MEL. *J. Phys. Chem. B* **101**, 9881–9885 (1997).
- 14. Pan, M. High resolution electron microscopy of zeolites. *Micron* 27, 219–238 (1996).
- 15. Millward, G. R., Ramdas, S., Thomas, J. M. & Barlow, M. T. Evidence for semi-regularly ordered sequences of mirror and inversion symmetry planes in ZSM-5/ZSM-11 shape-selective zeolitic catalysts. *J. Chem. Soc. Faraday Trans. 2 Mol. Chem. Phys.* **79**, 1075–1082 (1983).
- Zhang, H. et al. Open-Pore Two-Dimensional MFI Zeolite Nanosheets for the Fabrication of Hydrocarbon-Isomer-Selective Membranes on Porous Polymer Supports. Angew.
 Chemie Int. Ed. 55, 7184–7187 (2016).
- 17. Aramburo, L. R. *et al.* The porosity, acidity, and reactivity of dealuminated zeolite ZSM-5 at the single particle level: The influence of the zeolite architecture. *Chem. A Eur. J.* **17**, 13773–13781 (2011).
- 18. Anderson, M. W. & Klinowski, J. Direct observation of shape selectivity in zeolite ZSM-5 by magic-angle-spinning NMR. *Nature* **339**, 200–203 (1989).
- 19. John, N. S., Stevens, S. M., Terasaki, O. & Anderson, M. W. Evolution of surface morphology with introduction of stacking faults in zeolites. *Chem. A Eur. J.* **16**, 2220–2230 (2010).
- 20. Ugurlu, O. et al. Radiolysis to knock-on damage transition in zeolites under electron beam

- irradiation. Phys. Rev. B 83, 113408 (2011).
- 21. Mkhoyan, K. A., Maccagnano-Zacher, S. E., Kirkland, E. J. & Silcox, J. Effects of amorphous layers on ADF-STEM imaging. *Ultramicroscopy* **108**, 791–803 (2008).
- 22. Szostak, R., Pan, M. & Lillerud, K. P. High-resolution TEM imaging of extreme faulting in natural zeolite tschernichite. *J. Phys. Chem.* **99**, 2104–2109 (1995).
- 23. Terasaki, O. & Ohsuna, T. What can we observe in zeolite related materials by HRTEM? *Catal. Today* **23**, 201–218 (1995).
- 24. Pan, M. & Crozier, P. A. Quantitative imaging and diffraction of zeolites using a slow-scan CCD camera. *Ultramicroscopy* **52**, 487–498 (1993).
- 25. Bursill, L.A., Thomas, J. M. & Rao, K. J. Stability of zeolites under electron irradiation and imaging of heavy cations in silicates. *Nature* **289**, 157–158 (1981).
- Treacy, M. M. J. & Newsam, J. M. Electron beam sensitivity of zeolite L.
 Ultramicroscopy 23, 411–419 (1987).
- 27. Yoshida, K. & Sasaki, Y. Optimal accelerating voltage for HRTEM imaging of zeolite. *J. Electron Microsc. (Tokyo).* **62**, 369–375 (2013).
- 28. Kirkland, E. J. Advanced Computing in Electron Microscopy. vol. 40 (Springer US, 2010).
- 29. Treacy, M. M. J. Z dependence of electron scattering by single atoms into annulardark-field detectors. *Microsc. Microanal.* **17**, 847–858 (2011).
- 30. Gonzalez, R. C. Digital Image Processing. vol. 14 (2002).
- 31. Senftle, T. P. *et al.* The ReaxFF reactive force-field: development, applications and future directions. *npj Comput. Mater.* **2**, 15011 (2016).
- 32. Agrawal, K. V. *et al.* Oriented MFI Membranes by Gel-Less Secondary Growth of Sub-100 nm MFI-Nanosheet Seed Layers. *Adv. Mater.* **27**, 3243–3249 (2015).

- 33. Yuan, W., S. Lin, Y. & Yang, W. Molecular Sieving MFI-Type Zeolite Membranes for Pervaporation Separation of Xylene Isomers. *J. Am. Chem. Soc.* **126**, 4776–4777 (2004).
- 34. Zhu, X. *et al.* Establishing hierarchy: The chain of events leading to the formation of silicalite-1 nanosheets. *Chem. Sci.* 7, 6506–6513 (2016).
- 35. Rohling, R. Y., M. Szyja, B. & J. M. Hensen, E. Insight into the Formation of Nanostructured MFI Sheets and MEL Needles Driven by Molecular Recognition. *J. Phys. Chem. C* **123**, 5326–5335 (2019).

Author contributions

PK along with KAM and MT conceived the project. PK performed TEM data collection, analysis and developed the template matching algorithm with input from MT and KAM. HZ, QX and NR synthesized the 2D nanosheets. DWK prepared the MEL-containing directly synthesized nanosheets (in the presence of graphite) with input from MT and SG performed TEM characterization. NR and MS performed XRD and AFM measurements. NR synthesized membranes and with BM performed xylene membrane permeation measurements. HX and TD performed DFT simulations and along with KAM and PK interpreted the results on mechanical properties of the nanosheets. EOF and J.I.S. performed and analyzed the FPMD simulations for separation properties of the nanosheets. PK, MT and KAM prepared the manuscript with written contributions from all co-authors. KAM and MT co-directed all aspects of the project.

Corresponding authors

All correspondence and requests for materials should be directed to K. Andre Mkhoyan (<u>mkhoyan@umn.edu</u>) or Michael Tsapatsis (<u>tsapatsis@jhu.edu</u>) or P. Kumar (<u>kumar141@umn.edu</u>)

Acknowledgment

This work was primarily supported by the National Science Foundation (CBET-1705687). XRD was performed at Argonne National Laboratory supported by the U.S. Department of Energy, Office of Science, Office of Basic Energy Sciences, under Contract No. DE-AC02-06CH11357. Parts of this work were carried out in the Characterization Facility, University of Minnesota, that receives partial support from the NSF through the MRSEC and NNIN programs (DMR-1420013). The FPMD simulations used resources of the Argonne Leadership Computing Facility, which is a DOE Office of Science User Facility supported under Contract DE-AC02-06CH11357. Additional computer resources were provided by the Minnesota Supercomputing Institute. P.K. and E.O.F. acknowledges support from a Doctoral Dissertation Fellowship received from the Graduate School at the University of Minnesota. H.X. and T.D. acknowledge support from NSF 1332228. Q.X. acknowledges support from the National Natural Science Foundation of China (21471131).

Methods

Transmission electron microscopy. MFI nanosheet were prepared for TEM measurement by drop-casting a suspension of nanosheets in water on TEM grids (ultrathin carbon film on holey carbon support film, 400 mesh Cu, Ted Pella). The grid was air dried at room temperature before inserting in the TEM. For HAADF-STEM imaging, the TEM grid was further de-contaminated in a high vacuum-chamber for 9 hrs at 30° C. The sample was then transferred to the TEM with minimum exposure to air.

Bright-Field TEM (BF-TEM) images and selected area electron diffraction (SAED) patterns were collected on an FEI Tecnai G2 F30 (S)TEM with TWIN pole piece, a Schottky field-emission electron gun operating at 300 kV, 4000 V extraction voltage and equipped with a Gatan 4k×4k Ultrascan CCD. BF-TEM and diffraction data collection were performed under low electron dose (< 5 e⁻/Å²/s) to mitigate electron beam damage of the nanosheets. SAED patterns were acquired with near-parallel electron beam illumination and an acquisition time of 8 sec. BF-TEM images were acquired with an acquisition time of 1-2 sec.

ADF-STEM images were acquired in an aberration-corrected FEI Titan 60-300 (S)TEM, operating at 200 kV. Incident probe convergence angle was 21 mrad with < 20 pA screen current, 6 μ s/pixel dwell time, and 35 mrad ADF detector inner angle. For these measurements, the image pixel size was kept at 0.21 Å to minimize electron beam damage to the nanosheet. The total electron beam exposure area during image acquisition was 42.7 nm x 42.7 nm.

X-Ray diffraction and atomic force microscopy. Nanosheet coatings on silicon wafers were prepared according to a previously described method³⁶. 1.5 mL of a suspension of acid treated nanosheets (with structure directing agent, SDA partially removed) was carefully dropped on the

surface of the water in a Langmuir trough (Nima Liquid-Liquid trough with IU4 interface and Nima LB dipping mechanism, maximum area 120 cm², minimum area 23 cm²). After allowing ethanol to evaporate, the trough barriers were compressed at a speed of 30 cm²/min, until the surface pressure was increased to 25-30 mN/m. At this stage, a 1 cm x 1 cm square [100] oriented silicon wafer was lowered at a speed of 1 cm/min, with its flat surface parallel to the surface of the water. After contact was made, the wafer was raised up at the same speed and then left to dry. The sample was calcined at 500° C for 6 hours under 150 mL/min air flow.

In-plane synchrotron X-ray diffraction on calcined nanosheet samples was performed at beamline 33-BM-C at the Advanced Photon Source, Argonne National Laboratory. The incident X-ray source energy was 15.8 keV, corresponding to a wavelength of 0.78473Å. A Huber 6-circle diffractometer stage was used to position the sample at a grazing incidence angle of $<1^{\circ}$ to the incident beam. A collimator tube with slits of dimensions $1000\mu m \times 1000\mu m$ was used on the detector side. The diffracted beam was collected by a 2-dimensional area detector, scanning a 2θ range of 3-30 degrees with a step size of 0.01° . Helium atmosphere was maintained around the sample to minimize air scattering. The power law background (ax^b) was used for data fitting.

AFM measurements were carried out in AC mode in the repulsive regime using a Bruker Nanoscope V Multimode 8 AFM. Analysis of AFM images was carried out using Gwiddion 2.31 software.

Template matching. The process to find MFI and MEL unit cells in ADF-STEM images is implemented in four steps (Extended data Fig. 4) –

Step 1: To improve the visibility of the features in the image, a radial Wiener filter³⁷ was implemented to remove amorphous carbon background. Then, a band-pass (low-pass, high-pass)

filter was applied to eliminate high-frequency noise and low-frequency intensity variations in the image followed by convolution with a 5 X 5 pixel² matrix of ones to improve the signal-to-noise ratio (SNR)³⁰ (Extended data Fig. 2).

Step 2: ADF-STEM images of MFI and MEL unit cells in two different orientations were simulated using the *Multislice* algorithm²⁸. The defocus value of the probe was determined by matching simulated and experimental images (Extended data Fig. 3). The histograms of ADF intensities in simulated templates were matched to those in experimental ADF-STEM image. This was followed by normalized cross-correlation (NCC) of all four templates with the image to yield four two-dimensional NCC matrices of the same size as the image (one for each template) with intensity values within the limits of -1 to 1. Threshold value (I_{th}) was calculated by multiplying a confidence value (defined here as C = 0.8) with the maximum value in NCC matrix for each case. Values in the NCC matrices below I_{th} were set to zero. Following this, x, y coordinates of the maximum value of the local non-zero NCC points were assigned a template unit.

Step 3: The four NCC matrices for each template are then compared. If there are multiple identified templates at the same x, y coordinate, then two the highest NCC matrix values ($I_{NCC,th}$) were compared and, if the difference between the two values is greater then a *trust* value (defined here as 0.04) then the template with the highest NCC value is assigned at that location, otherwise, no template is assigned.

Step 4: Identified units for each MFI and MEL (two orientations each) are then cross-correlated and averaged to yield four experimental unit cell images³⁸. If cross-correlated experimental unit cell image does not have any of the four unit cell features, then it is not used further.

Steps 2 to 4 are repeated with new experimental unit cells and with 85% confidence value (C = 0.85) and *trust* value of 0.01 for all the analyzed images, and the results are displayed in main text

Fig. 2 and Extended data Fig. 5. The template matching process described above was also applied on BF-TEM images shown in Extended data Fig. 7.

TEM data simulation. ADF-STEM and SAED patterns were simulated using the Multislice code^{28,39}. The unit cell size of MFI along **a-**, **b-**, and **c-**direction used in simulations is 20.02 Å, 19.90 Å, 13.38 Å, respectively. The unit cell size of MEL along **a-**, **b-**, and **c-**direction used in simulations is 20.07 Å, 20.07 Å, 13.41 Å, respectively. ADF-STEM images with defocus series was simulated for one unit cell of MFI and MEL (see Extended data Fig. 3) at beam energy $V_o = 200 \text{ kV}$, spherical aberration coefficient $Cs_3 = 0 \text{ mm}$, $Cs_5 = 0 \text{ mm}$, convergence angle $\alpha = 21 \text{ mrad}$, defocus Δf ranging from -20 Å to 200 Å in steps of 20 Å. Specimen transfer function (atomic potential) and probe function pixelation of $1024 \times 1024 \text{ pixel}^2$, slice thickness of 1 Å, ADF detector inner angle of 35 mrad and outer angle of 317 mrad were used. The output ADF-STEM images had 256 x 256 pixel² with 0.09 Å/pix in both **a-** and **c-**direction, which is of the same order or larger than room temperature RMS atomic displacement (or thermal vibrations amplitude) of Si and O: $us_i = 0.1156 \text{ Å}$ and uo = 0.0637 Å. Since thermal vibrations of the atoms in these simulations has negligible effect, the frozen phonons were not included.

ED patterns were simulated using an $V_o = 300$ kV electron beam ($Cs_3 = 2.0$ mm, $Cs_5 = 0$ mm, $\alpha = 0$ mrad for nearly parallel probe, probe defocus $\Delta f = 1000$ Å) with a 2048 x 2048 pixel² grid for nanosheets with the overall size of 11 u.c, 1.5 u.c. and 20 u.c. along **a-**, **b-** and **c-**direction (Extended data Fig. 9). Simulated ADF-STEM images were convolved with a Gaussian function of FWHM 1 Å to include the effect of source size. Diffraction patterns were convolved with a Gaussian function of FWHM 1.2 pixel to account for thermal diffuse scattering and slight beam convergence.

XRD data simulation. Powder XRD pattern was simulated for MFI with varying MEL content using DiFFaX code⁴⁰ (Extended data Fig. 1). The unit cell size of MFI along **a-, b-,** and **c-**direction used in simulations is 20.04 Å, 19.92 Å, 13.39 Å, respectively. The unit cell size of MEL along **a-, b-,** and **c-**direction used in simulations is 20.07 Å, 20.07 Å, 13.41 Å, respectively. The X-ray wavelength used for simulations was kept same as the experiment at 0.78473 Å. Pseudo-Voigt instrumental broadening was used for simulating the data. Patterns were simulated for 0-10% MEL content within the MFI framework.

Quantification of MEL content in nanosheets. For estimation of MEL content (102) and (101) spot intensities in SAED patterns were quantified. The intensity of diffraction spot was calculated by (i) gaussian peak fit to the spot and (ii) sum of intensities of pixels in an area of 23 X 42 pixel² enclosing the spot using 2D Gaussian function of the form, $y = a_1 e^{-(x-x_0)^2} \frac{(y-y_0)^2}{2\sigma y^2} + a_2$, where a_I is the gaussian peak height, x_0 , y_0 are the centers of the gaussian, σ_x , σ_y are the standard deviations along the \mathbf{x} - and \mathbf{y} -direction and a_2 is the background. For gaussian peak fit the intensity of the spot is calculated as the volume under the gaussian ($V = 2\pi a_1\sigma_x\sigma_y$). The calculated intensity ratios (I_{102}/I_{101}) for nanosheet models (Extended data Fig. 9) are plotted for both the methods in Extended data Fig. 9d. A linear fit (%MEL = -193.2 * $I_{102}/I_{101} + 94.7$) is used to best estimate the variation in I_{102}/I_{101} vs % MEL. Experimental diffraction patterns were classified according to the streaking of (102) spots. 50 different patterns showed varying level of streaking of (102) spots. All the patterns were aligned and added to yield average pattern (Extended data Fig. 10d). The intensity ratios (I_{102}/I_{101}) evp were calculated by fitting a 2D Gaussian function as described above

(Extended data Fig. 10e). This ratio was used to calculate the *%MEL* in the nanosheets from the calibration plot.

Simulated XRD patterns were used to create a I_{102}/I_{101} vs % MEL plot (Extended data Fig. 1b) using the maximum values of the peaks. A 2nd order polynomial fit (% MEL = I_{102}/I_{101})² - I_{102}/I_{101}) + 27.6) was used to create a calibration curve for MEL content estimation. I_{102}/I_{101} of 0.07 was measured from in-plane XRD data by measuring the maximum values for (102) and (101) peak. This ratio was used to calculate the %MEL in the nanosheets from the calibration plot.

Mechanical Properties and Structural relaxations. The atomistic simulations presented in Fig. 4 (main text) and Supplementary Fig. 2, were carried out with the code LAMMPS⁴¹ using the classical ReaxFF potential³¹ based on the Si, O, and H parameters of Newsome et al.⁴². The structures were considered relaxed when the force on each atom measures less than 0.001eV/Å. To verify the classical description of the complex bond lengths and angles, we have compared the ReaxFF and Density Functional Theory (DFT) description of an MFI unit cell comprising 288 atoms, Supplementary Fig. 2. The first-principles DFT calculations were carried out using the Vienna *ab initio* Simulations Package (VASP)^{43,44}. The Kohn-Sham equations were solved using the projected-augmented wave (PAW) method⁴⁵ along with standard PAW potentials for the Si and O atoms⁴⁶. The Perdew-Burke-Ernzerhof (PBE) exchange-correlation functional was selected for structural optimizations⁴⁷. The Brillouin-zone integrations were performed at the Γ point due to the large crystal cell. The kinetic energy cutoff for plane waves was set to default value ~ 520 eV. The convergence criterion for electronic self-consistency was set to 10⁻⁵ eV, and the "accurate" precision setting was adopted to avoid wrap around errors. Both lattice vectors and atoms were

fully relaxed until the force components on atoms were smaller than 10^{-2} eV/Å. In Supplementary Fig. 2a,b we present a histogram comparison of bond lengths and bond angles measured from the MFI structure computed with the two methods. The small discrepancy on reproducing the correct bond lengths can be explained that during the ReaxFF force field development, the focus is on reproducing the DFT reaction energies and reaction barriers.

In the ReaxFF calculations of the in-plane Young's modulus Y, fully optimized 2D zeolite structures were compressed by ε =0.1%, 0.3%, 0.6%, 0.8%, and 1% along the desired periodicity direction. During re-optimizations, only the lattice vector along the compression strain was kept fixed, while all the other parameters were relaxed. The force tolerance during relaxation was also set to 0.001eV/Å. The reported Y was extracted by fitting the elastic energy E vs ε data to the equation $\frac{E}{V} = 0.5 \, Y \varepsilon^2$, where V is the volume of the cell used in the calculation. In computing V, the 2D layer thickness was taken as 3.06 nm for MFI, 3.08 nm for MFI, and 3.07 nm for the MFI-MEL heterostructures. These values were based on the thickness measurements performed on the relaxed atomistic structures.

First principles molecular dynamics (FPMD) simulations for p-/o-xylene diffusivity. Potentials of mean force (PMFs, dF) for p-xylene and o-xylene diffusion were obtained from FPMD simulations in the canonical ensemble using umbrella sampling (with harmonic umbrella potentials of the form $V(r_{\xi}) = 1/2k_{\rm u}(r_0 - r_{\xi})^2$) and the weighted histogram analysis method (WHAM)⁴⁸. The PMFs were expressed as a function of the ξ coordinate of sorbate center-of-mass along the straight channel (trans-membrane direction), and $\xi = 0$ and 1 correspond to the channel intersections. A 3-nm film (with 2 unit cells along the a-direction and 1 unit cell along the c-direction consisting of 288 Si atoms, 592 O atoms, 32 H atoms) was modeled using FPMD

simulations with the CP2K software suite,⁴⁹ the PBE exchange-correlation functional,^{47,50} GTH pseudopotentials,⁵¹ a double zeta basis set,⁵² a 400 Ry cutoff for the auxiliary plane wave basis, and Grimme D3 dispersion correction.⁵³ The temperature was controlled using Nosé-Hoover^{54,55} chain⁵⁶ thermostats at 573 K. The geometric center of the benzene ring was restrained to equally spaced umbrella windows of 0.5 Å with $k_u = 200 \text{ kJ mol}^{-1} \text{ Å}^{-2}$, and in each umbrella window, at least 5 ps of production with a time step of 0.5 fs were used for analysis (Supplementary Fig. 3).

Nanosheet Selectivity. Diffusivity of p-xylene (D^p) and o-xylene (D^o) is defined as $A^p \cdot e^{\frac{-dF^p}{RT}}$, and $A^o \cdot e^{\frac{-dF^o}{RT}}$, respectively, where R is the gas constant, T is the temperature, A is the preexponential factor, dF is the PMFs for diffusion of p-xylene (p) or o-xylene (p) along the straight channel in a given type of pore. The flux p (mol/m²-s) for p-xylene across a nanosheet (Supplementary Fig. 4a,b) having volume fractions of MFI, MEL and interface pores p and p and p and p and p are the properties of the properties of the flux p and p are the properties of p and p are the properties of the p

$$\begin{split} J^p &= J^p_{MFI} + J^p_{MEL} + J^p_{INT} \\ \\ J^p &= -\alpha_{MFI} D^p_{MFI} \frac{\Delta c}{t} - \alpha_{MEL} D^p_{MEL} \frac{\Delta c}{t} - \alpha_{INT} D^p_{INT} \frac{\Delta c}{t} \\ \\ &= -(\alpha_{MFI} D^p_{MFI} + \alpha_{MEL} D^p_{MEL} + \alpha_{INT} D^p_{INT}) \frac{\Delta c}{t} = -(D^p_{MFI-MEL}) \frac{\Delta c}{t} \end{split}$$

where Δc is loading difference across a nanosheet of thickness t. For the same Δc across the membrane, the nanosheet selectivity (NS), defined here as the ratio of permeance of p-xylene over o-xylene and can be written as

$$NS = \frac{\alpha_{MFI} D_{MFI}^p + \alpha_{MEL} D_{MEL}^p + \alpha_{INT} D_{INT}^p}{\alpha_{MFI} D_{MFI}^o + \alpha_{MEL} D_{MFI}^o + \alpha_{INT} D_{INT}^o}$$

If R^p and R^o are defined as the ratio of diffusivity in pure MFI over diffusivity in MEL containing nanosheets for p-xylene and o-xylene, respectively:

$$R^p = \frac{D_{MFI}^p}{D_{MFI-MEL}^p} = \frac{D_{MFI}^p}{\alpha_{MFI}D_{MFI}^p + \alpha_{MEL}D_{MEL}^p + \alpha_{INT}D_{INT}^p},$$

$$R^{o} = \frac{D_{MFI}^{o}}{D_{MFI-MEL}^{o}} = \frac{D_{MFI}^{o}}{\alpha_{MFI}D_{MFI}^{o} + \alpha_{MEL}D_{MEL}^{o} + \alpha_{INT}D_{INT}^{o}},$$

Then, the nanosheet selectivity, NS, can be written in terms of R^o and R^p as follows:

$$NS = \frac{R^o}{R^p} \cdot \frac{D_{MFI}^p}{D_{MFI}^o} = \frac{R^o}{R^p} \cdot \left[(e^{\frac{-dF^p}{RT}})/(e^{\frac{-dF^o}{RT}}) \right] \cdot \left[A^p/A^o \right]$$
 Equation 1

At 573K, $[(e^{\frac{-dF^p}{RT}})/(e^{\frac{-dF^o}{RT}})]$ is calculated as 1100 for MFI and 3.6x10⁸ for MEL. NS for $\alpha_{MFI}=1$, and for $\alpha_{MEL}=1$ is then 1100 and 3.6x10⁸ times $[A^p/A^o]$, respectively (Table S2). For the calculations of NS for MEL-containing MFI nanosheets (Table S2), we assume that the pre-exponentials A^p and A^o depend only on the isomer and do not depend on the structure being MFI, INT or MEL.

Membrane Selectivity. The flux (*J*) through a uniform MFI membrane of thickness *L* and loading difference Δc can be written as $J = -D_{MFI} \frac{\Delta c}{L}$ (Supplementary Fig. 4c). If the same thickness *L* is now divided into sections with thickness L_i ($\sum_{i=1}^n L_i = L$) and diffusivity D_i , then flux through the membrane can be written as $J' = -D_i \frac{\Delta c_i}{L_i}$. This expression can be rearranged into $\frac{\Delta c_i}{J'} = -\frac{L_i}{D_i}$ such that

$$\frac{\sum_{i=1}^{n} \Delta c_i}{J'} = -\sum_{i=1}^{n} \frac{L_i}{D_i} \Rightarrow \frac{\Delta c/L}{J'} = -\sum_{i=1}^{n} \frac{L_i/L}{D_i}$$

Considering the same Δc across the same thickness L, for the uniform MFI membrane and the one made by sections of diffusivity D_i , and setting the thickness ratio L_i/L equal to the volume fraction of the corresponding section, x_i , we get:

$$\frac{J/D_{MFI}}{J'} = \sum_{i=1}^{n} \frac{x_i}{D_i} \quad \Rightarrow \quad \frac{J}{J'} = \sum_{i=1}^{n} \frac{x_i}{D_i/D_{MFI}}$$

For a membrane of total thickness L that is made by stacking a fraction (x) of MEL-containing nanosheets $(\alpha_{MEL} > 0$, diffusivity $D_{MFI-MEL})$ and a fraction (I-x) of pristine MFI $(\alpha_{MEL}, \alpha_{INT} = 0$, diffusivity D_{MFI}) nanosheets we have:

$$\frac{J}{J'} = \frac{1 - x}{D_{MFI}/D_{MFI}} + \frac{x}{D_{MFI-MEL}/D_{MFI}} \quad \Rightarrow \quad \frac{J}{J'} = (1 - x) + x \cdot R$$

Using the subscripts, p and o, for para- and ortho-xylene, respectively we have:

$$\frac{J^p}{J^{p'}} = (1 - x) + x \cdot R^p \text{ and } \frac{J^o}{J^{o'}} = (1 - x) + x \cdot R^o$$

The selectivity $(MS'=J^p'/J^o')$ for a membrane containing a fraction x of MEL-containing nanosheets is related to the selectivity of a pure MFI membrane $(MS=J^p/J^o)$ as follows:

$$\frac{MS'}{MS} = \frac{(1-x) + x \cdot R^o}{(1-x) + x \cdot R^p}$$
 Equation 2

We note that MS is equal to NS for $\alpha_{MFI}=1$, which was calculated as 1,100 times A^p/A^o . We also note that the total MEL content of such membrane is written as $x \cdot \alpha_{MEL}$. Selectivity calculations for membranes with different MEL content performed using the formula above are shown in Table S3.

Data availability. The authors declare that the main data supporting the findings of this study are available within the article and its Supplementary Information files. Extra data are available from the corresponding authors upon request.

Code availability. The template matching code used to identify MFI and MEL is available from the K.A. Mkhoyan and P. Kumar upon reasonable request.

References

- 36. Rangnekar, N. *et al.* 2D zeolite coatings: Langmuir-Schaefer deposition of 3 nm thick MFI zeolite nanosheets. *Angew. Chemie Int. Ed.* **54**, 6571–6575 (2015).
- 37. Kilaas, R. Optimal and near-optimal filters in high-resolution electron microscopy. *J. Microsc.* **190**, 45–51 (1998).
- 38. Frank, J. The Role of Correlation Techniques in Computer Image Processing. in *Computer Processing of Electron Microscope Images* (ed. Hawkes, P. W.) 187–222 (Springer Berlin Heidelberg, 1980).
- 39. Cowley, J. M. & Moodie, A. F. The scattering of electrons by atoms and crystals. I. A new theoretical approach. *Acta Crystallogr.* **10**, 609–619 (1957).
- 40. Treacy, M. M. J., Newsam, J. M. & Deem, M. W. A gereral recursion method for calculating diffracted intenisties from crytsals containing planar stacking faults. *Proc. R. Soc. Lond. A* **433**, 499–520 (1991).
- 41. Plimpton, S. Fast parallel algorithms for short-range molecular dynamics. *Journal of Computational Physics* vol. 117 1–19 (1995).
- 42. Newsome, D. A., Sengupta, D., Foroutan, H., Russo, M. F. & van Duin, A. C. T.

 Oxidation of Silicon Carbide by O₂ and H₂ O: A ReaxFF Reactive Molecular Dynamics

 Study, Part I. *J. Phys. Chem. C* 116, 16111–16121 (2012).
- 43. Kresse, G. & Hafner, J. Ab initio molecular dynamics for liquid metals. *Phys. Rev. B* 47, 558–561 (1993).
- 44. Kresse, G. & Furthmüller, J. Efficient iterative schemes for ab initio total-energy calculations using a plane-wave basis set. *Phys. Rev. B Condens. Matter Mater. Phys.* **54**, 11169–11186 (1996).

- 45. Blöchl, P. E. Projector augmented-wave method. *Phys. Rev. B* **50**, 17953–17979 (1994).
- 46. Joubert, D. From ultrasoft pseudopotentials to the projector augmented-wave method. *Phys. Rev. B Condens. Matter Mater. Phys.* **59**, 1758–1775 (1999).
- 47. Perdew, J. P., Burke, K. & Ernzerhof, M. Generalized gradient approximation made simple. *Phys. Rev. Lett.* **77**, 3865–3868 (1996).
- 48. Grossfield, A. WHAM: The weighted histogram analysis method, version 2.0.9. http://membrane.urmc.rochester.edu/content/wham (2013).
- 49. Hutter, J., Iannuzzi, M., Schiffmann, F. & Vandevondele, J. Cp2k: Atomistic simulations of condensed matter systems. *Wiley Interdiscip. Rev. Comput. Mol. Sci.* **4**, 15–25 (2014).
- 50. Perdew, J. P., Burke, K. & Ernzerhof, M. Generalized gradient approximation made simple. *Phys. Rev. Lett.* 77, 3865–3868 (1996).
- 51. Hartwigsen, C., Goedecker, S. & Hutter, J. Relativistic separable dual-space Gaussian pseudopotentials from H to Rn. *Phys. Rev. B* **58**, 3641–3662 (1998).
- 52. VandeVondele, J. & Hutter, J. Gaussian basis sets for accurate calculations on molecular systems in gas and condensed phases. *J. Chem. Phys.* **127**, 114105 (2007).
- 53. Grimme, S., Antony, J., Ehrlich, S. & Krieg, H. A consistent and accurate ab initio parametrization of density functional dispersion correction (DFT-D) for the 94 elements H-Pu. *J. Chem. Phys.* **132**, 154104 (2010).
- 54. Nosé, S. A unified formulation of the constant temperature molecular dynamics methods. *J. Chem. Phys.* **81**, 511–519 (1984).
- 55. Hoover, W. G. Canonical dynamics: Equilibrium phase-space distributions. *Phys. Rev. A* **31**, 1695–1697 (1985).
- 56. Martyna, G. J., Klein, M. L. & Tuckerman, M. Nosé-Hoover chains: The canonical

ensemble via continuous dynamics. J. Chem. Phys. 97, 2635–2643 (1992).

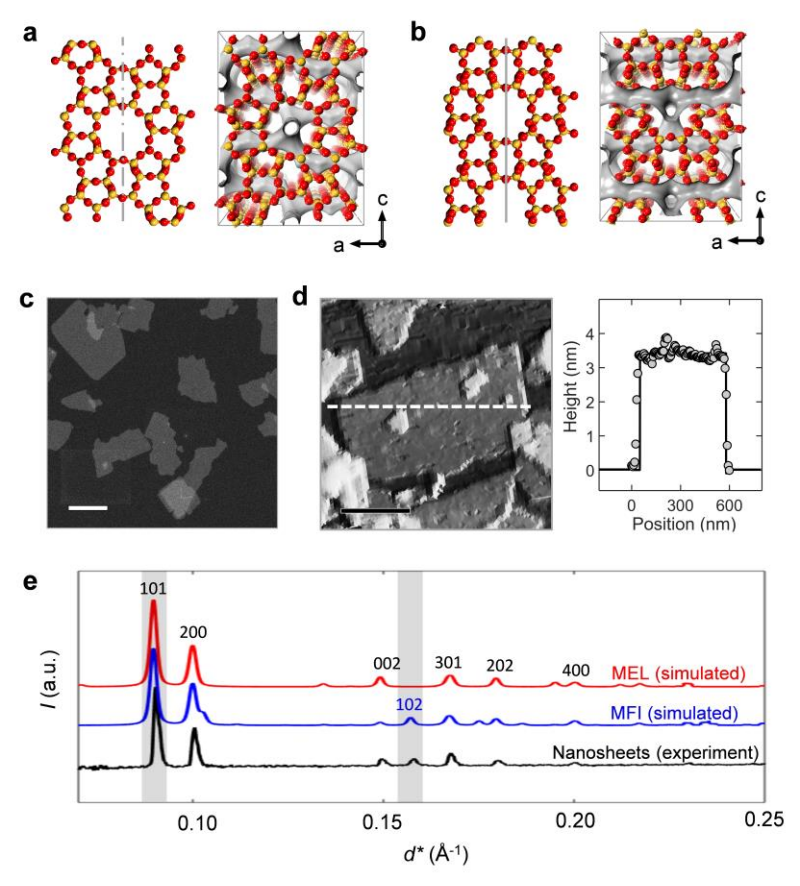


Figure 1. Structure of nanosheet. Atomic structure (left) and the resulting porous network shown in grey (right), for **a**, MFI and **b**, MEL viewed along the **b**-direction that are formed by connecting pentasil chains through inversion symmetry (dashed grey line) and mirror symmetry (solid grey line), respectively. **c**, ADF-STEM image of MFI nanosheets **d**, AFM image of an MFI nanosheet. Line scan (dotted white line) across the nanosheet is plotted in the right panel. The average measured thickness of the nanosheet along **b**-direction is 3.2 nm. **e**, In-plane XRD pattern of bout-of-plane oriented nanosheet monolayer (only h0l-reflections are detected) is plotted with simulated powder XRD pattern for MFI and MEL (all reflections are included). The (102) peak is unique to MFI structure and is highlighted in grey. The ratio of intensities of the (102) peak over that of the (101) peak is used to estimate the volumetric content of MEL as 4.3 % (see Extended data Fig. 1). Scale bars in c and d are 200 nm.

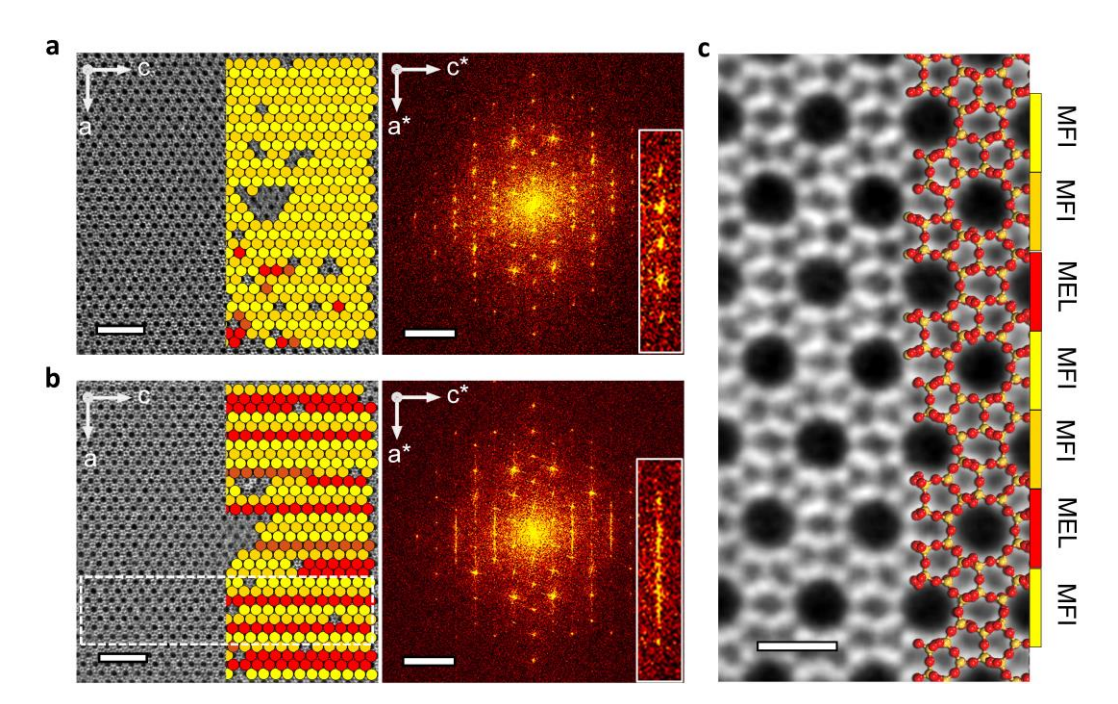


Figure 2. Identification of MFI and MEL heterostructures in nanosheets. Filtered ADF-STEM image (left) and the FFT (right) for an area **a**, with typical MFI structure and **b**, with MEL domains intergrown within MFI framework. Overlaid on ADF-STEM images are colored circles for MFI (yellow) and MEL (red) unit cells that are identified using a template matching algorithm described in detail in methods and Extended data Fig. 4. Insets in FFT show streaking of a periodic set of spots which are an indication of finite MFI domains limited in size along the **a**-direction. **c**, Cross-correlated and averaged ADF-STEM section of MFI-MEL heterostructure from the dotted region shown in b. The atomic structure is overlaid on top of the ADF-STEM image with perfect registration of atoms in the model with the bright dots (representing silicon atoms) in the image. Scale bars in a, b are 5 nm for ADF-STEM image, 2 nm⁻¹ for FFT, and in c is 1 nm.

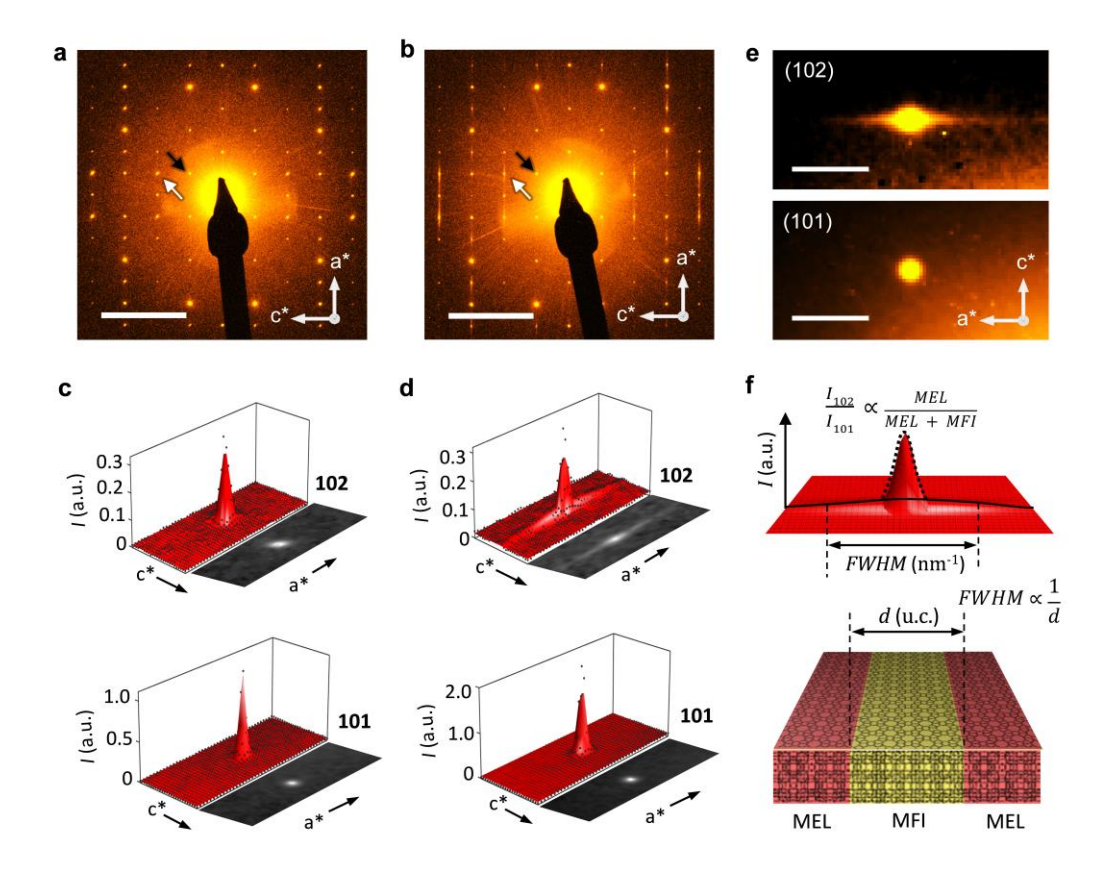


Figure 3. Electron diffraction analysis for quantification of MEL in MFI nanosheets. [010] zone axis SAED pattern for **a**, MFI nanosheet with typical circular spots and for **b**, MFI nanosheets with MEL domains showing streaking of h+l=odd diffraction spots. Black and white arrows indicate (101) and (102) spots, respectively. **c-d**, 2D Gaussian fits shown as red surfaces for (102) and (101) spots from SAED patterns in a and b, respectively. Black dots indicate experimental intensity values of the diffraction spots shown in the adjacent panels in black and white. **e**, Sum averaged (102) and (101) spot for 50 MFI-MEL heterostructured (MEL-containing) nanosheets. **f**, Schematic for a 2D gaussian peak showing full-width-at-half-maximum (*FWHM*) and intensity (*I*) ratio of (102) and (101) spots used to determine MFI domain size along **a**-direction and volumetric content of MEL, respectively. Scale bars in a, b are 2 nm⁻¹ and e are 0.2 nm⁻¹.

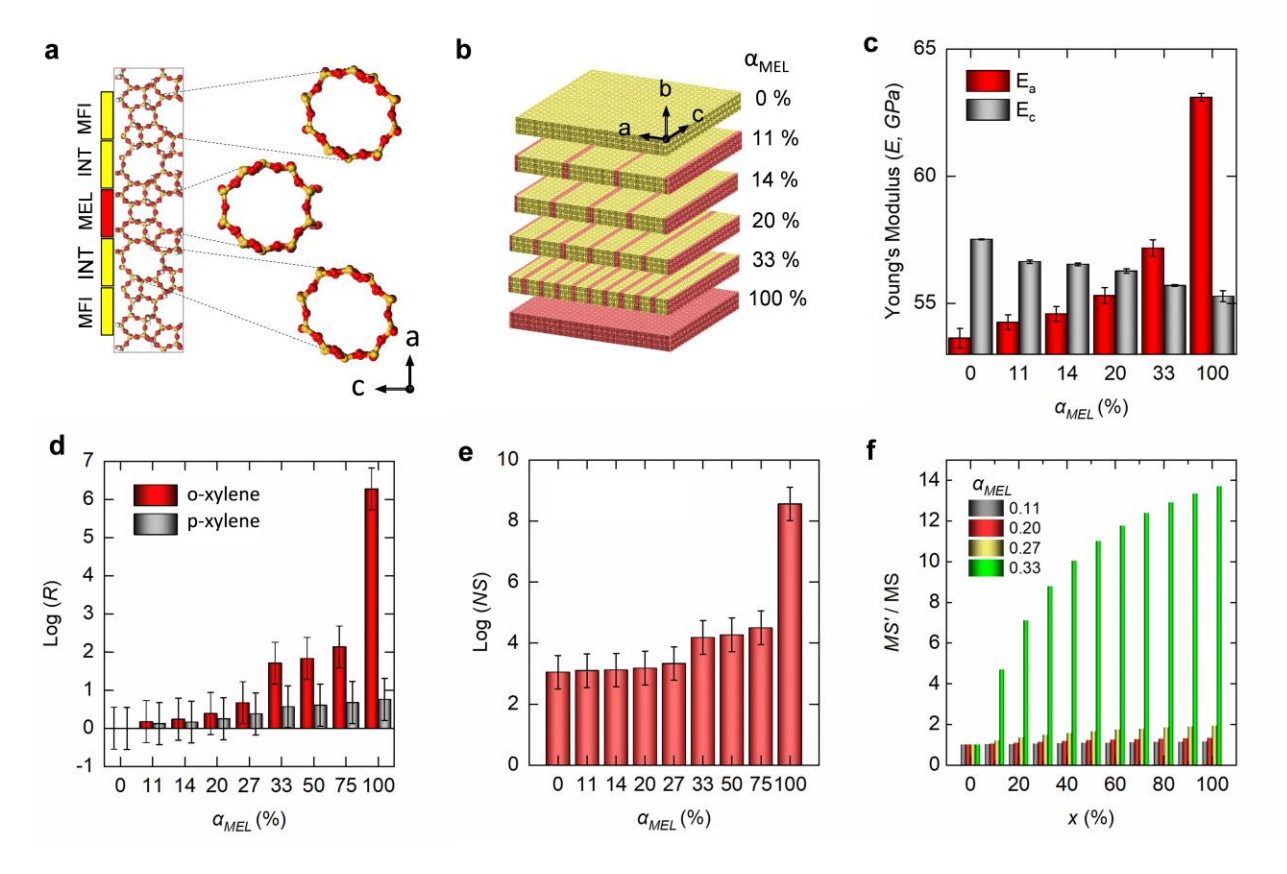


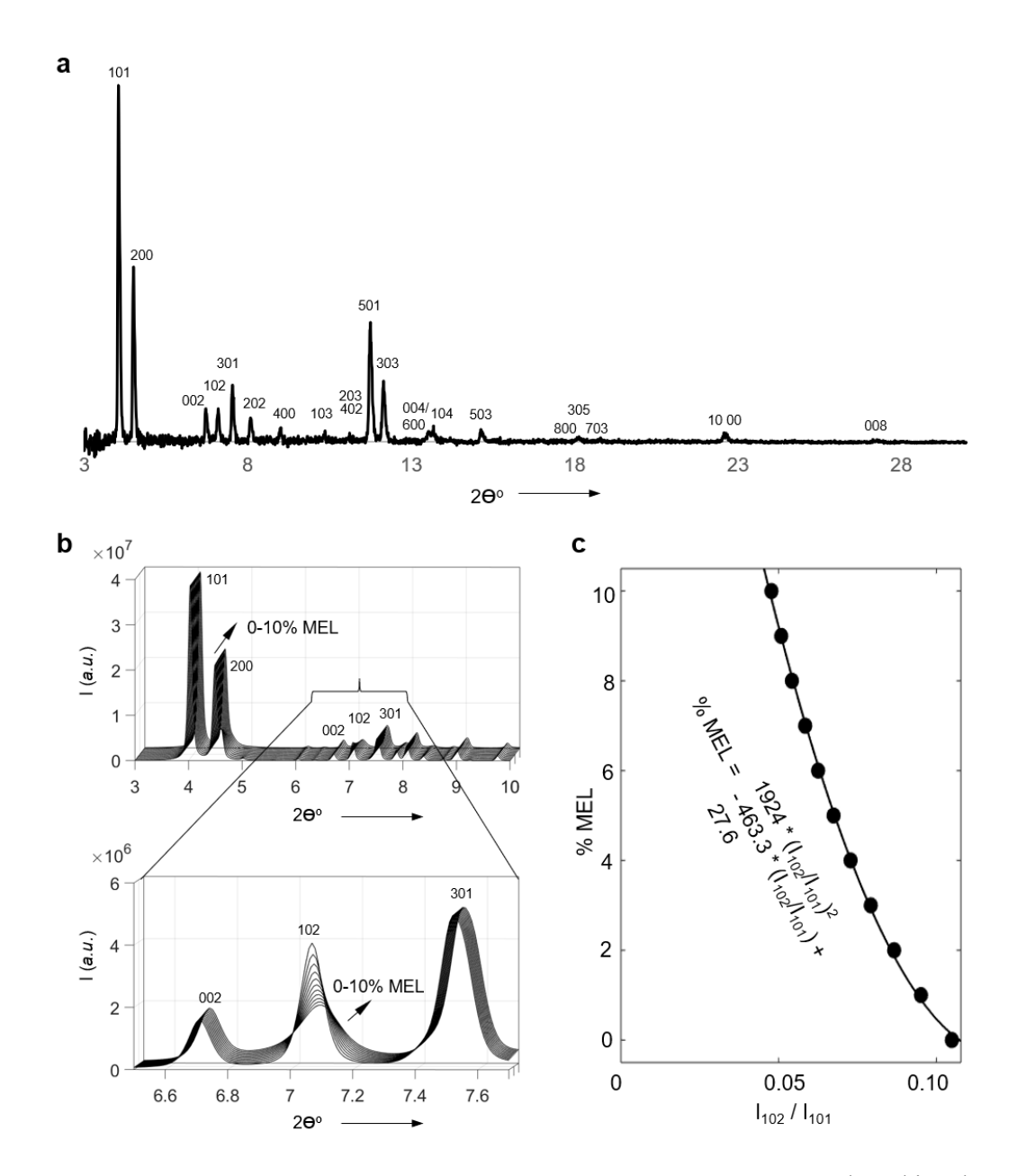
Figure 4. Effect of MEL domains on separation and mechanical properties of the MFI nanosheet. a, Atomic structure of a single MEL unit cell domain fully connected to MFI unit cells with magnified views of the resulting MFI, MEL and interfacial (INT) pores. The heterostructure is periodic along a- and c-directions and is 1.5 unit cells thick along the b-direction. b, Knittings of 2D-MFI (yellow) and 1D-MEL (red) nanosheet heterostructures with increasing MEL content α_{MEL} . The interface pores are MFI type and highlighted in yellow for clarity. c, Young's Moduli obtained upon compression of the structures shown in b along a- and c-directions. d, Calculated diffusivity ratios: R^p , para-xylene in pure MFI over MEL-containing nanosheet; R^o , ortho-xylene in pure MFI over MEL-containing, for each model shown in b. e, Calculated diffusivity ratios of p-xylene/o-xylene denoted as nanosheet selectivity (NS), for each structure shown in b. Error bars in d and e correspond to 3 kJ/mol uncertainty in the potentials of mean force. f, Selectivity enhancement for membranes (MS'/MS) consisting of a stack of nanosheets vs the fraction (in %) of MEL-containing nanosheets for various MEL content, α_{MEL} , in nanosheet (see table S3).

Table 1. Membrane permeation properties.

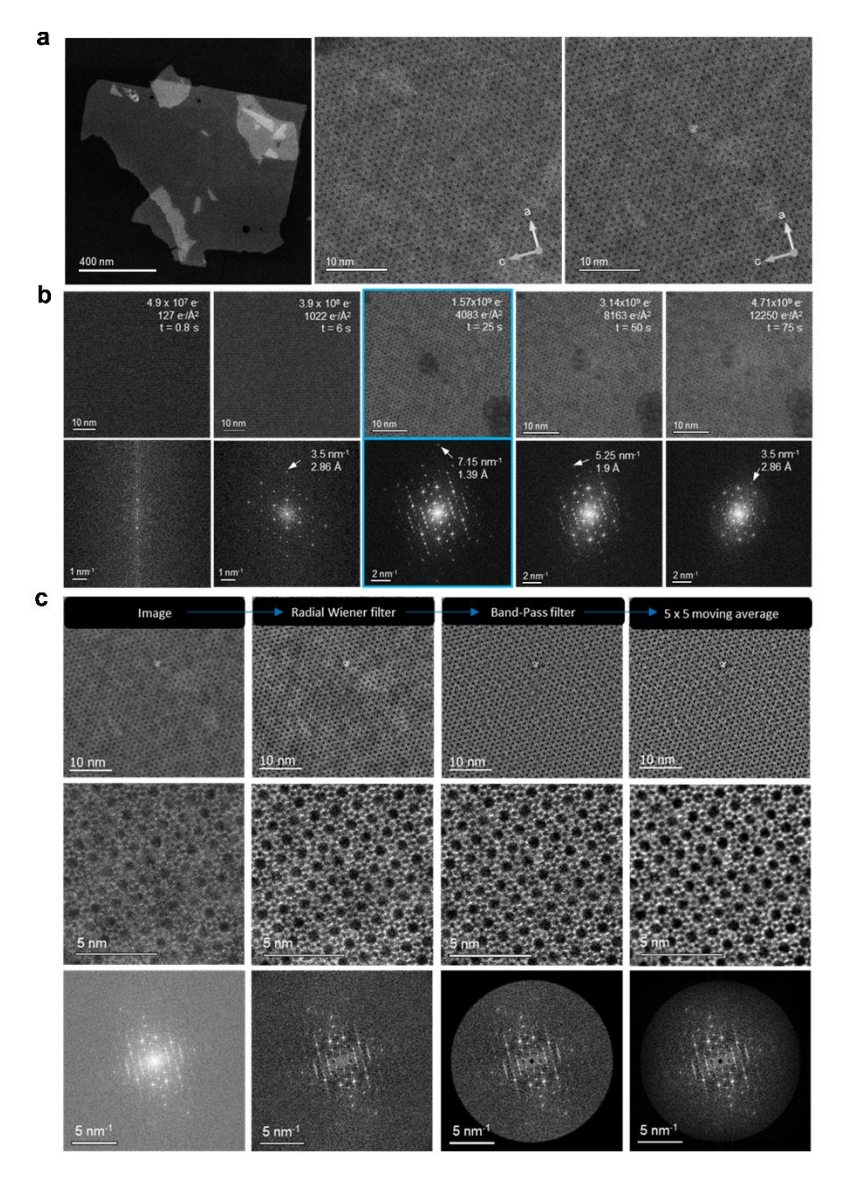
Membrane code	Feed pressure (kPa)*		Temperature	Para-xylene Flux	Mixture Separation
	Para- xylene	Ortho- Xylene	(°C)	$(\text{mol/m}^2\text{-s x }10^3)$	Factor (permeate/feed molar ratios)
M1	47.5	47.5	300	0.47	60
M1	95	95	300	0.24	19.3
M2	47.5	47.5	275	0.40	61

^{*}Molar composition 47.5% para-xylene, 47.5% ortho-xylene, 5% 1,3,5-trimethyl benzene.

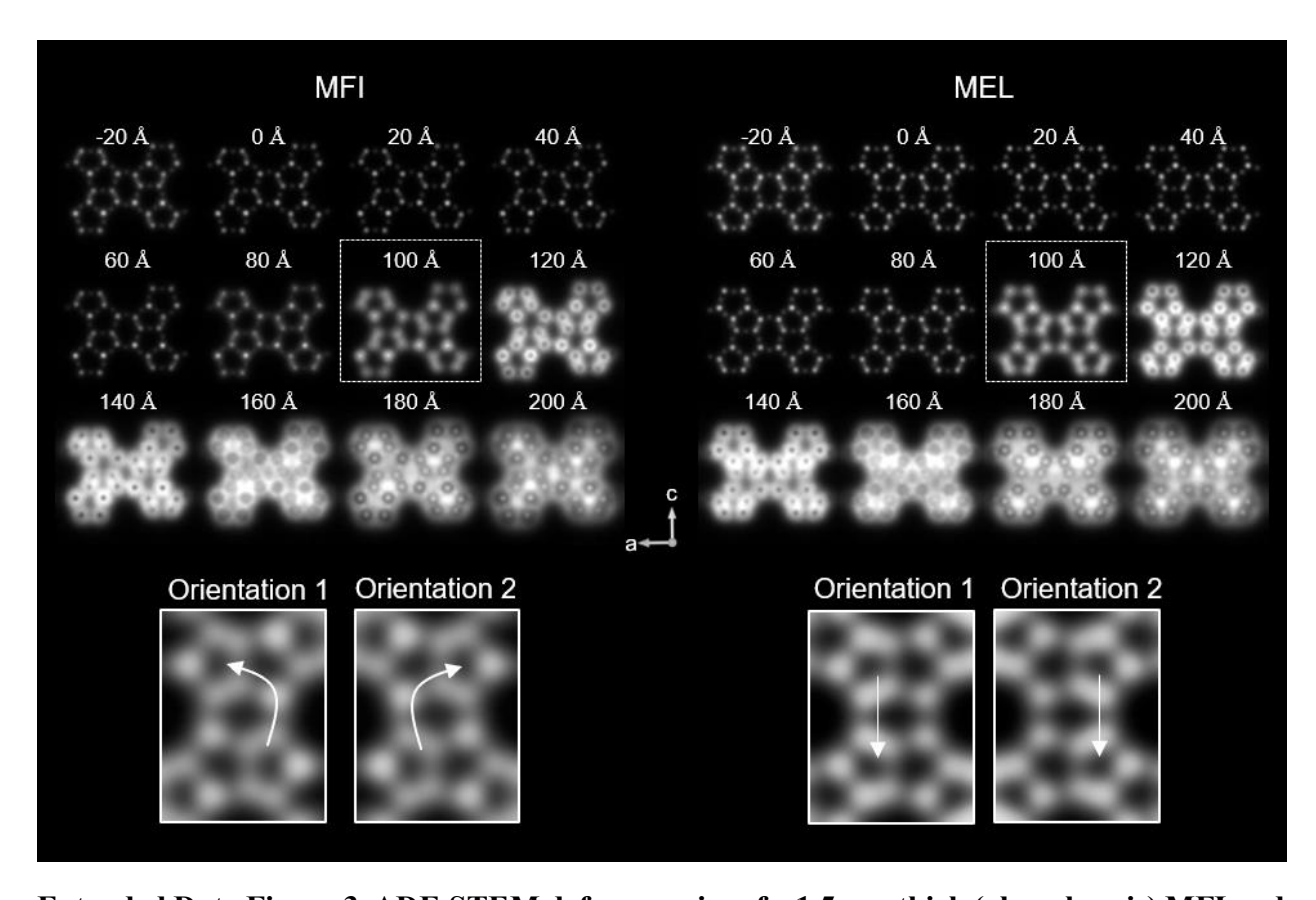
Extended Data Figures



Extended Data Figure 1. MEL content quantification through XRD. a, Indexed in-plane XRD data after background removal is labeled with corresponding peak positions. b, Bulk powder XRD patterns for MFI with 0-10% MEL are simulated using DiffaX computer code. The (102) peak decreases in intensity with increasing MEL content (bottom panel) while the (101) peak remains unchanged. c, Calibration curve from simulated data is plotted for % MEL vs I_{102}/I_{101} . Using the fitted curve, the MEL content of the entire sample is calculated: the experimentally determined I_{102}/I_{101} ratio is 0.07, which corresponds to 4.3% MEL content.

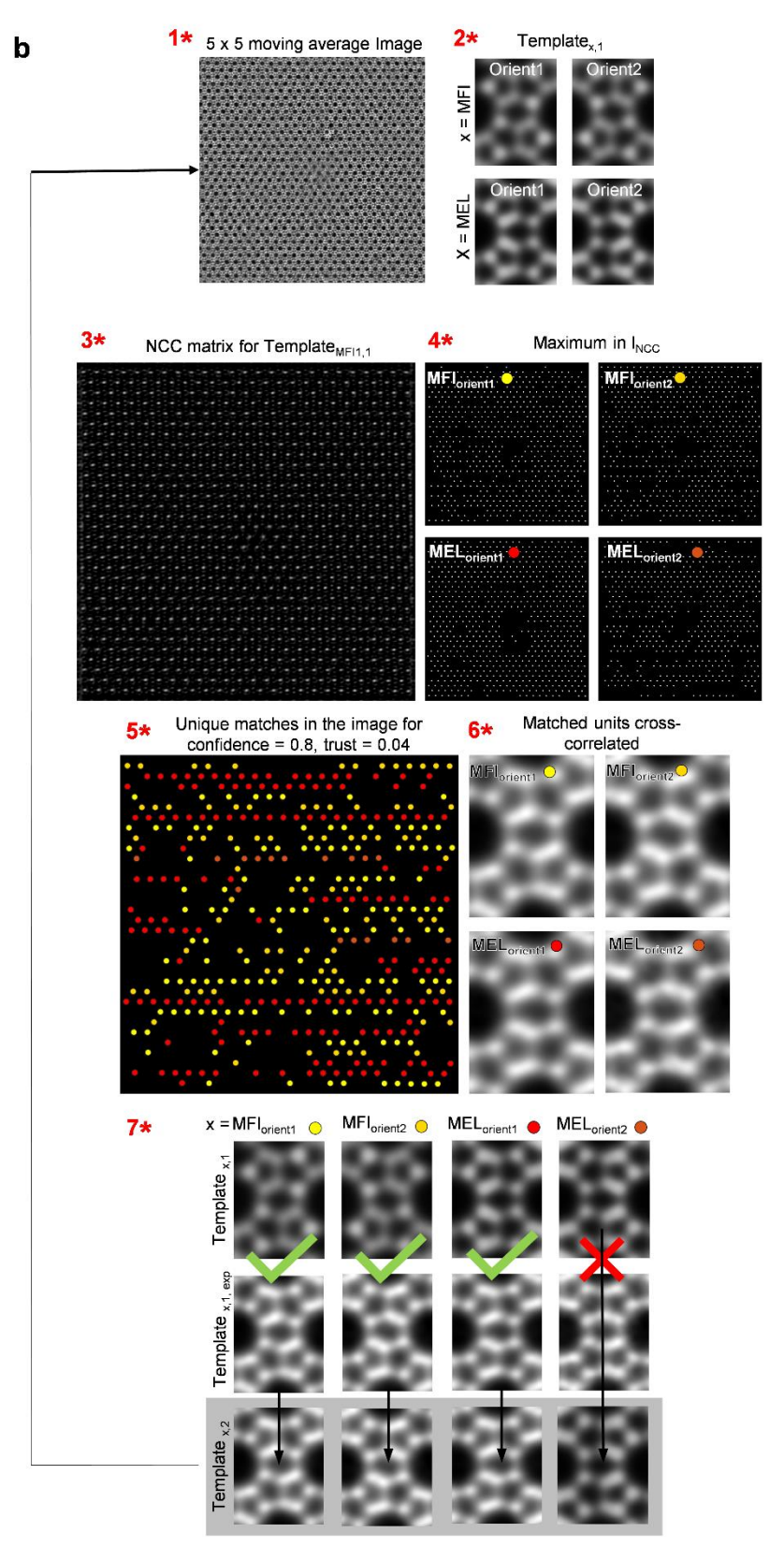


Extended Data Figure 2. ADF-STEM imaging of MFI nanosheets. a, (left panel) Low magnification ADF-STEM image of an MFI nanosheet deposited on a carbon support. (middle and right panel) As-acquired raw ADF-STEM images of the sections shown in main text (Fig. 2 a,b). **b,** ADF-STEM image (top) and the corresponding FFT (bottom) at increasing electron doses (left to right). Image acquired at the optimal dose is highlighted in blue. At less than 1.6×10^9 e⁻, pores are barely visible (missing FFT spots as compared to FFT on right), while at higher doses the nanosheet is amorphized as seen by the disappeared spots in FFT (when compared to FFT on left). Cumulative electrons (e⁻), electron dose (e⁻/Å²) and the total time of exposure (t) for image acquisition are listed at the top right corner of the as-acquired images. Maximum detectable periodicity is indicated by the arrows in FFT. **c,** Filtering steps (Left to right) for as-acquired raw image are shown. The same filtering steps are implemented as step 1 in template matching algorithm described in Extended data Fig. 4. Top row shows the ADF-STEM images. Middle row shows a smaller section from the image on top. Bottom column is the fast-fourier transform (FFT) of the image.



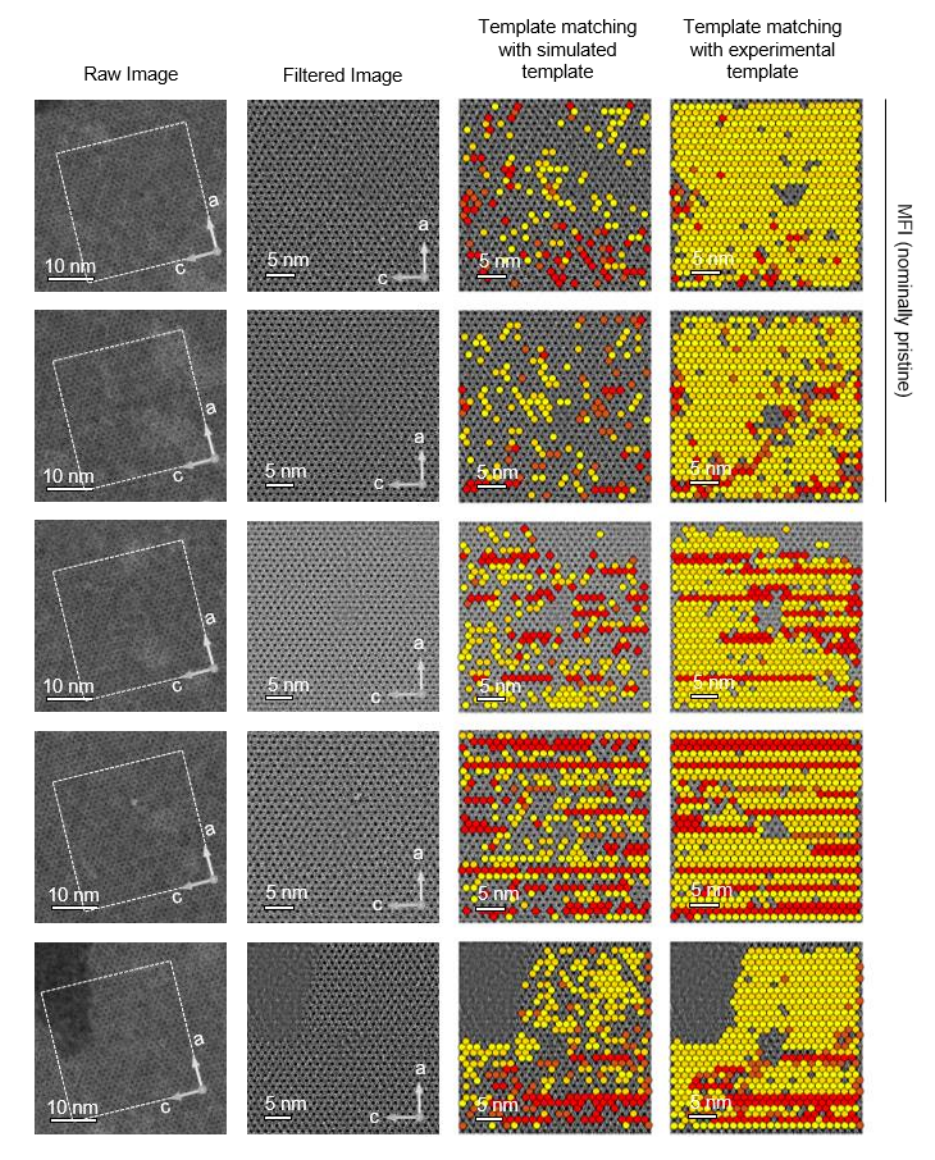
Extended Data Figure 3. ADF-STEM defocus series of a 1.5 u.c. thick (along b-axis) MFI and MEL unit cell. The simulation parameters were: Cs = 0 mm, $V_o = 200$ kV, $\Delta f = -20$ to 200 Å, 35 and 317 mrad for ADF detector inter- and outer-angles, 256 x 256 pix image size. The frozen phonons were not included in these calculations. $\Delta f = 100$ Å simulated image (enclosed by dotted lines) matched the experimental defocus conditions and is used as starting template (shown at the bottom after Gaussian blurring) for the template matching algorithm described in Extended data Fig. 4. Each simulated image is scaled in intensity individually from 0 to 255.

 $Template_{x,n+1} = Template_{x,n,exp}$

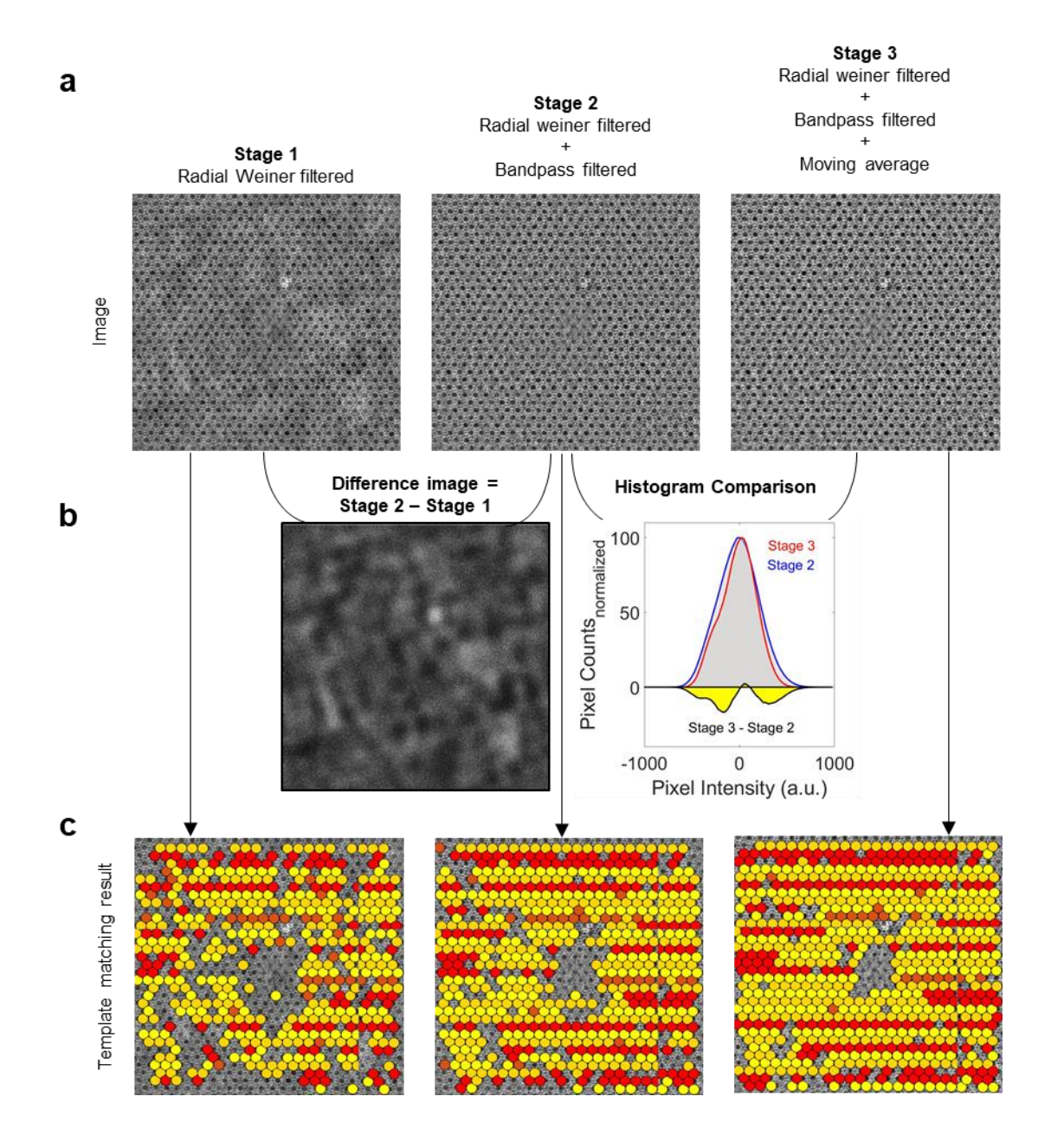


Extended Data Figure 4. Algorithm for finding MFI and MEL distribution across ADF-STEM.

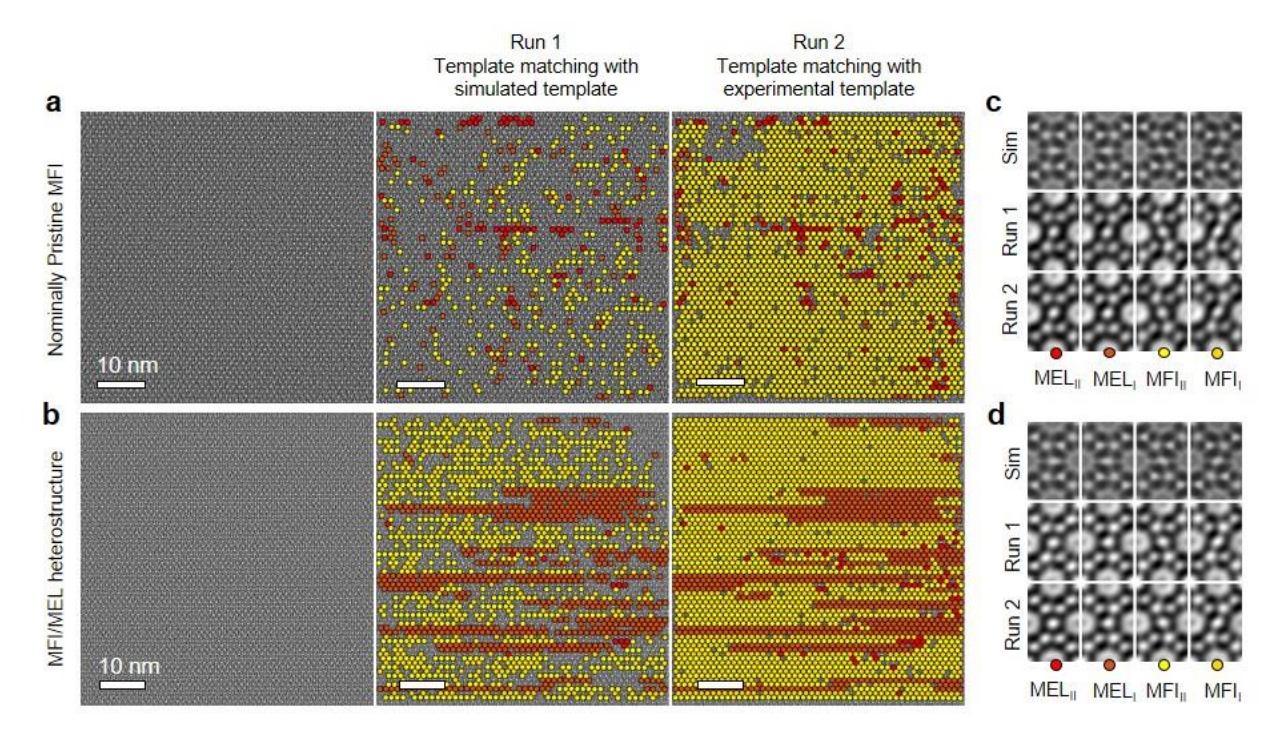
Demonstration of the cross-correlation based template matching code (written in MATLAB) to find multislice simulated MFI and MEL template in TEM images. a, Flowchart describing the four steps (bound by grey boxes) for executing the algorithm. b, Representative outputs of the code from the locations marked as 1* - 7* in the flowchart shown in a.



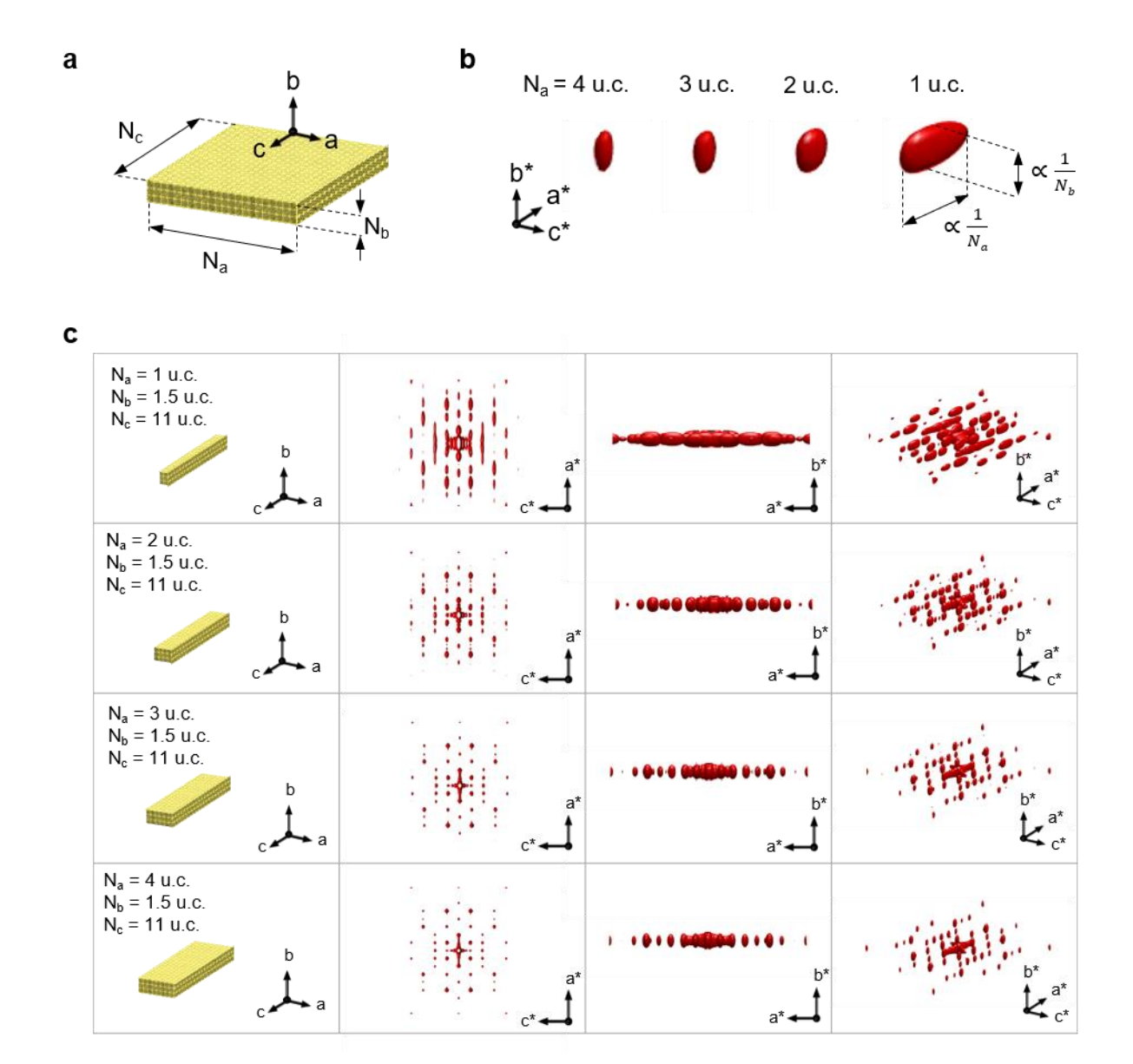
Extended Data Figure 5. Results of template matching algorithm on different ADF-STEM images. As-acquired raw images from the microscope are shown on the left. Dotted lines represent the section which is aligned with a- and c-axes of the crystal as vertical and horizontal lines respectively. Filtered images processed using radial Wiener, Band-pass, and moving 5x5 average filters of the section shown in the first column are shown in the second column. Results of the template matching algorithm are shown in the third and fourth column with shades of red and yellow circles representing two different orientations of MEL and MFI, respectively (same color scheme as in the Extended data Fig. 4b and main text Fig. 2a). Third column images are obtained by cross-correlation of simulated unit-cell TEM images of MFI and MEL, with the filtered images in column 2, while the fourth column is obtained by cross-correlating the (cross-correlated and averaged) templates created from the matched units of each color in the third column with the corresponding images in column 1. Fourth column shows more complete filling since the scanned templates are created from the experimental image, thereby incorporating the noise levels and astigmatism present during collection of experimental data.



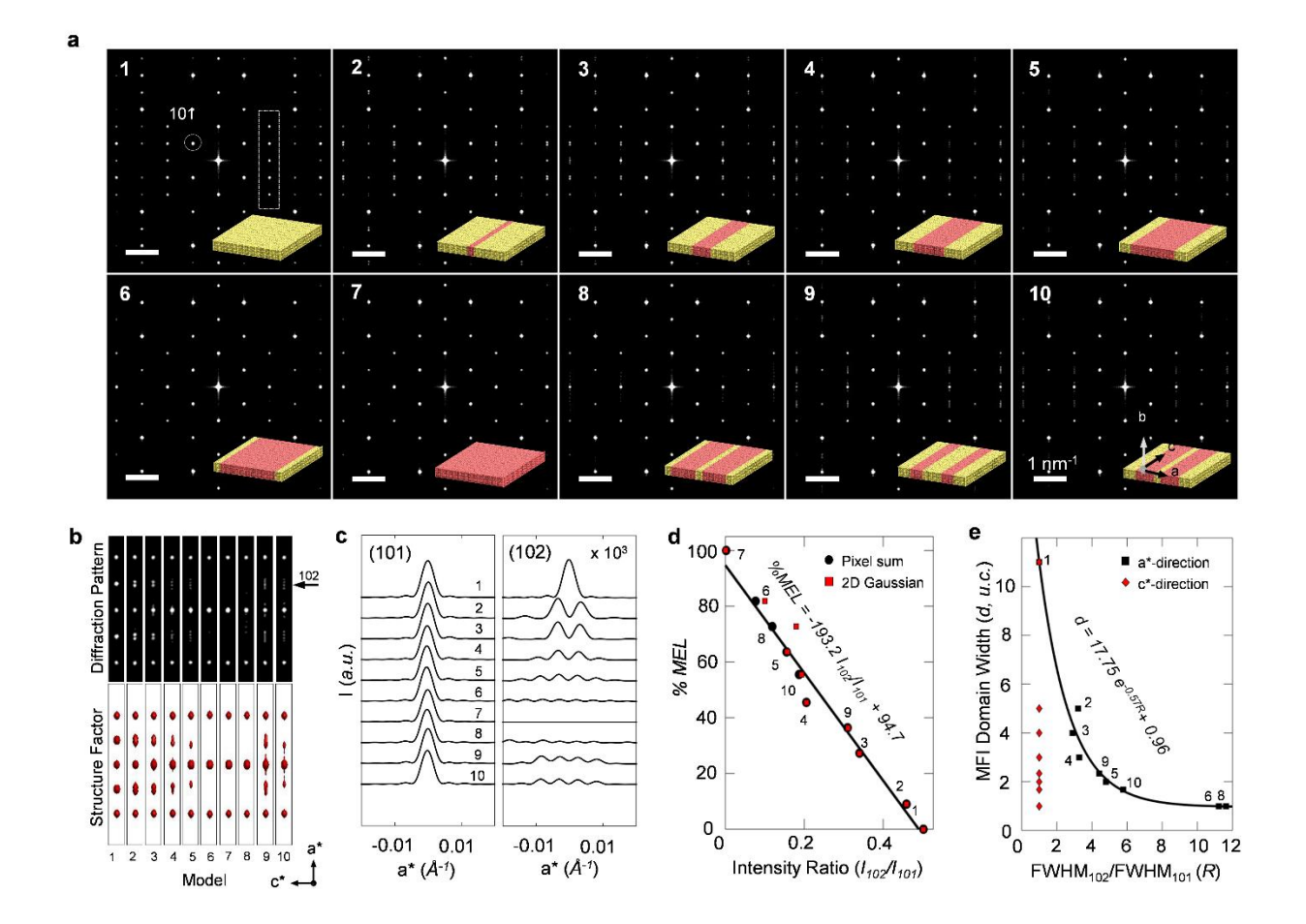
Extended Data Figure 6. Effect of different stages of filtering an ADF-STEM image on template matching. a, ADF-STEM at different stages of filtering. **b,** Effect of each stage of filtering on the ADF-STEM images. Difference image between Stage 2 and Stage 1 shows a low-frequency intensity variation arising due to the carbon residues on the nanosheet. Histogram of the image at Stage 3 shows a decrease in FWHM by 14% as compared to histogram of the image at Stage 2. **c,** Results of the template matching algorithm (algorithm is shown in extended data figure 4) at each stage of filtering show that the aforementioned reduction in FWHM correspond to a decrease in the noise in image.



Extended Data Figure 7. Template matching results for BF-TEM images. Filtered BF-TEM images (first column), template matching results using simulated MFI and MEL unit cell images (second column) and results using templates created from the matched units in run 1 (third column) for **a**, nominally pristine MFI nanosheet **b**, MFI-MEL nanosheet. Simulated and cross-correlated experimental units extracted from **c**, panels a for MFI nanosheet and **d**, panels b for MFI-MEL nanosheet. First row indicates the simulated BF-TEM templates used for run 1. Second and third rows indicate the cross-correlated and averaged units identified after run 1 and 2, respectively.

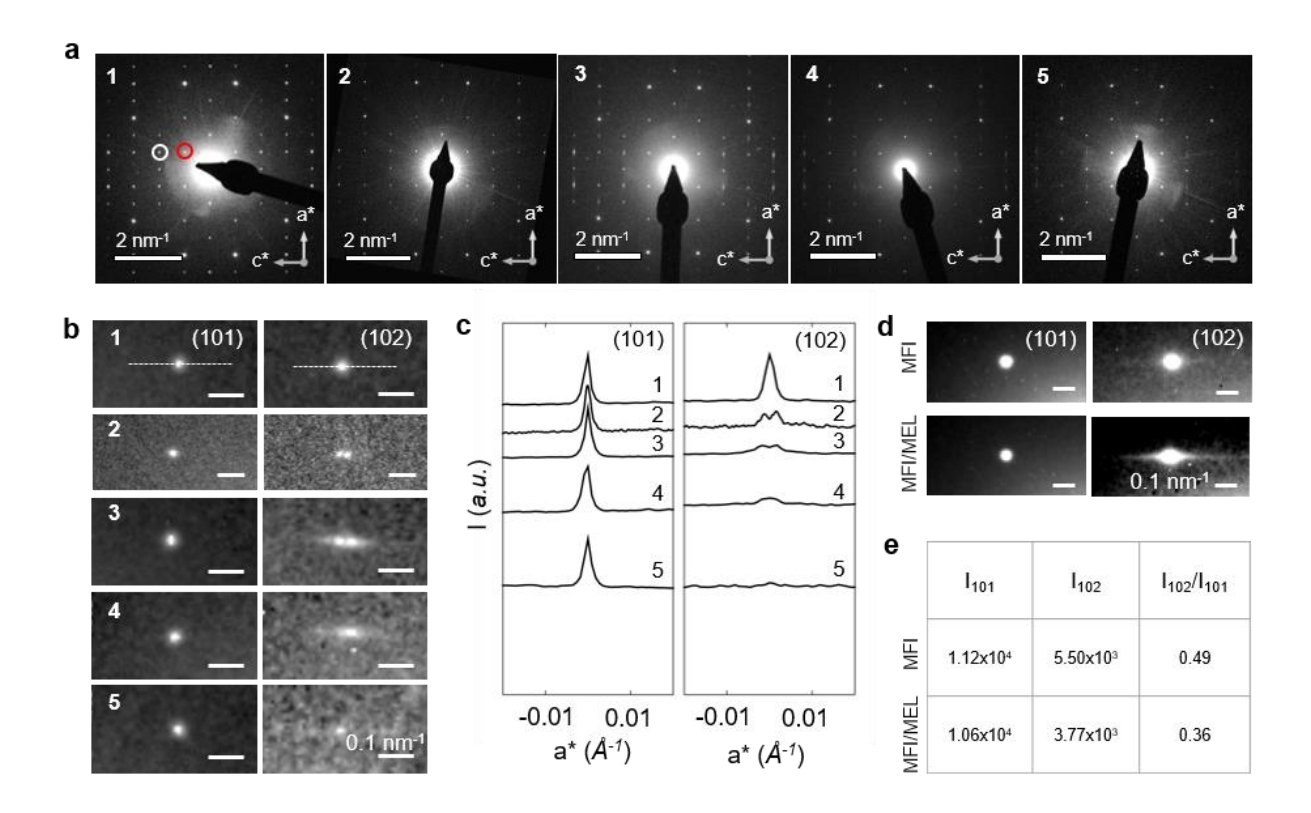


Extended Data Figure 8. Effect of domain size on the reciprocal space of MFI nanosheet. a, 3D model of a MFI nanosheet with lengths along a-, b-, and c-direction as N_a , N_b , and N_c unit cells (u.c.). b, Changes in shape of the structure factor iso-surface at a reciprocal lattice point are shown, as the length of the MFI supercell is changed along a-direction from 1-4 u.c. The width of the reciprocal lattice point along a*- and b*- direction is inversely proportional to length along a- and b-direction (N_a , N_b). c, MFI supercells ($N_a = 1-4$ u.c., $N_b = 1.5$ u.c., $N_c = 11$ u.c.) along with different projections of the corresponding structure factor iso-surfaces in the 3D reciprocal space are shown. It is seen that as the length of the MFI supercell increases in a-direction, the elongation of the spot in a* - direction decreases. This corroborates with the streaking of spots along a* direction in acquired electron diffraction patterns.



Extended Data Figure 9. Simulation of ED patterns for various nanosheet heterostructures.

a, ED patterns simulated using multislice code for nanosheet heterostructures shown in bottom right of each panel. Total length of the heterostructure along a-, b-, and c-direction is 11 u.c., 1.5 u.c. and 20 u.c. **b,** Diffraction pattern section indicated by dotted line in panel a is shown in a magnified view (top row) for models 1-10. Iso-surfaces for structure factor, $|F|^2$ are plotted for the same models (bottom row). **c,** Line scans from $|F|^2$ taken across (101) and (102) spot along a*-direction show changes in intensity of (102) spot while (101) spot remains unchanged as the MEL content and domain size varies. **d,** *Intensity ratio* vs % *MEL* content in the heterostructures (1 to 10) shows linear variation (line fit has R^2 =0.98). Intensities of individual spots are calculated by adding up the pixel values (or area under the 2D gaussian fit) for each spot after background subtraction. **e,** MFI domain width along a-direction (*d*) vs FWHM of (102) peak over FWHM of (101) peak (*R*) for heterostructures (1 to 10) shows exponential variation (fit has R^2 =0.97). FWHM is calculated along a*- and c*-direction by fitting a 2D-Gaussian function.



Extended Data Figure 10. Analysis of experimental SAED patterns. a, Representative SAED patterns showing variation in diffraction spots across different nanosheets. (101) spot is highlighted in red and (102) spot is highlighted in white. b, (101) and (102) spots from SAED patterns in panel a are magnified and shown. Streaking and splitting of (102) spots is seen while the corresponding (101) spot shows minimal variations in shape and intensity. c, Line-scans across diffraction spots shown in panel b are plotted. Linescans 2 and 3 show splitting of spots with distance along a* between the peaks being 0.0027 Å-¹ and 0.0036 Å-¹. This splitting indicates the presence of a repeating heterostructure in the nanosheet which has a periodicity of 37 nm and 28 nm respectively. d, Averaged (101) and (102) spots are shown from SAED patterns of 50 MFI nanosheets and 50 MFI-MEL nanosheets. e, Intensities of diffraction spots shown in panel d are listed in the table, with MFI nanosheets having 0% MEL and MFI-MEL nanosheets having 25% MEL. Percentage of MEL is calculated using the calibration chart (I_{102}/I_{101} vs %MEL) shown in Extended data Fig. 9d.

Supplementary Information

One-Dimensional-Intergrowths in Two-Dimensional Zeolite Nanosheets and their Effect on Ultra-Selective Transport

Prashant Kumar¹*, Dae Woo Kim^{1,2,¶}, Neel Rangnekar^{1,¶}, Hao Xu^{4,¶} Evgenii O. Fetisov^{5,¶}, Supriya Ghosh¹, Han Zhang¹, Qiang Xiao⁶, Meera Shete¹, J. Ilja Siepmann^{1,5}, Traian Dumitrica⁴, Benjamin McCool⁷, Michael Tsapatsis^{1,8,9}*, K. Andre Mkhoyan¹*

(Corresponding authors*: kumar141@umn.edu, tsapatsis@jhu.edu, mkhoyan@umn.edu)
(¶ indicates equal contribution)

¹ Department of Chemical Engineering and Materials Science, University of Minnesota, Minneapolis, MN

² Department of Chemical and Biomolecular Engineering, Korea Advanced Institute of Science and Technology, Daejeon 305-701, Republic of Korea

³ School of Chemical Engineering, Chonnam National University, Buk-gu, Gwangju, 61186 Republic of Korea

⁴ Department of Mechanical Engineering, University of Minnesota, Minneapolis, MN

⁵ Department of Chemistry and Chemical Theory Center, University of Minnesota, Minneapolis, MN

⁶ Key Laboratory of the Ministry of Education for Advanced Catalysis Materials, Institute of Physical Chemistry, Zhejiang Normal University, Jinhua, Zhejiang, China

⁷ Separations and Process Chemistry, Corporate Strategic Research, ExxonMobil Research and Engineering, Annandale, NJ 08801, USA

⁸ Department of Chemical and Biomolecular Engineering & Institute for NanoBioTechnology Johns Hopkins University, 3400 N. Charles Street, Baltimore, MD 21218 (USA)

⁹ Applied Physics Laboratory, Johns Hopkins University, 11100 Johns Hopkins Road, Laurel, MB 20723 (USA)

Table of Contents

- 1. ML-MFI synthesis and exfoliation.
- 2. Purification of MFI nanosheets.
- 3. MFI membrane fabrication procedure.
- 4. Xylene isomer separation measurements.
- 5. Direct synthesis of MEL-containing MFI nanosheets in the presence of graphite.
- 6. De-lamination of MEL-containing MFI nanosheets by melt-compounding
- 7. Supplementary Figures 1-7
- 8. Table S1-S3

1. ML-MFI synthesis and exfoliation. Multilamellar silicalite-1 (ML-MFI) was synthesized according to the previously reported procedure.¹ The structure directing agent (SDA) was a diquaternary ammonium surfactant [C₂₂H₄₅-N+(CH₃)₂-C₆H₁₂-N+(CH₃)₂-C₆H₁₃](OH)₂] or C₂₂₋₆-6(OH)₂, synthesized by alkylation of N,N,N',N'-tetramethyl-1,6-hexanediamine with 1-bromodocosane at 70°C followed by alkylation of the resultant product by 1-bromohexane at 85°C. C₂₂₋₆₋₆(OH)₂ was obtained by ion exchange of the bromide salt. ML-MFI was synthesized from a gel with composition 100 SiO₂:15 C₂₂₋₆₋₆(OH)₂:4000 H₂O:400 EtOH. After hydrolysis for 24 hours at room temperature, hydrothermal growth was carried out by transferring the gel to a rotating Teflon-lined steel autoclave at 150 °C for 5 days. After centrifugation, the cake was washed with distilled water to reduce the pH to 9 and dried in a vacuum oven at 130 °C.

ML-MFI was exfoliated by melt compounding to obtain polymer-zeolite nanocomposite.^{2,3}In a typical exfoliation process, 3.84 g of polystyrene (Mw = 45000 g/mol) and 0.16 g of the dried ML-MFI were manually mixed and loaded in a vertical, corotating twin screw extruder with a recirculation channel (DACA mini compounder). The mixture was blended sequentially at 120 °C for 20 min, 170 °C for 25 min, 150 °C for 30 min and 200 °C for 20 min under a nitrogen environment and at a screw speed of 300 rpm. The MFI-nanosheet nanocomposites were then extruded out at 150 °C.

2. Purification of MFI nanosheets. Purified MFI nanosheet coating suspension was obtained according to the previously reported procedure.³ 3.0 g of exfoliated nanocomposite was dispersed in toluene to yield 1.0% w/w suspension by sonication in a bath sonicator (Branson 5510R-DTH, 135 watts) for 30 min. The resulting suspension was centrifuged (Beckman Coulter, Avanti J-20 XP equipped with JA25.50 rotor) in four 50 mL FEP centrifuge tubes at 40,000 g for 3 h to sediment zeolite nanosheets at the bottom of the centrifuge tubes. Sedimented nanosheets were

separated from the supernatant and redispersed in toluene. The centrifugation and re-dispersion process was repeated twice. The resulting nanosheet sediment was then dispersed in 20 mL toluene, and placed on top of 20 mL chlorobenzene in a 50 mL FEP centrifuge tube, drop by drop by a transfer pipette, to create a nonlinear one step density gradient. Centrifugation was carried out at 40,000 g for 3 h. At the end of centrifugation, the nanosheets sedimented at the bottom of the centrifuge tube were collected by pouring out the supernatant. The zeolite sediment obtained after removal of polystyrene was dispersed in 20 mL n-octanol by horn sonication (Qsonica Q500, 500 watts, 0.12500 microtip operating at 20% of maximum amplitude) for 3 min followed by sonication in the bath sonicator for 30 min. A nonlinear multilayered density gradient was created in a 50 mL FEP centrifuge tube by sequentially placing 5 mL chloroform (q 5 1.48 g/cc), 5 mL dichloromethane (q 5 1.33 g/cc), 10 mL chlorobenzene (q 5 1.10 g/cc), and finally 20 mL nanosheet suspension in octanol. After centrifugation at 12,000 g for 30 min, half of the top fraction (n-octanol) was collected and diluted to 40 mL and centrifuged at 40,000 g for 3 h to sediment the purified nanosheets. The sedimented nanosheets were dispersed in 40 mL n-octanol by the horn sonication for 3 min followed by sonication in the bath sonicator for 60 min. This suspension was characterized by TEM and high-resolution TEM (HRTEM) and used for fabrication of nanosheet films.

3. MFI membrane fabrication procedure. MFI nanosheet membranes were made similar to the previously reported procedure.⁴ Here, the support preparation method was modified to increase mechanical strength. For each membrane support, 1.9 g of quartz fiber powder was mixed with 0.5 mL of silicon carbide precursor (StarPCS SMP-10, StarFire Systems) in hexane (precursor:hexane = 1:4 by volume). The precursor mixture was prepared in a glove box to prevent exposure of the silicon carbide precursor to the atmosphere. The compacts were sintered at 1100 °C for 4 hours (at

a heating and cooling ramp rate of 4 °C/min) under a nitrogen flow of 50 sccm. The supports were then polished with 600 grit followed by 1200 grit SiC polishing paper (Buehler), and sonicated (Branson 5510R-DTH, 135 watts) in deionized (DI) water for 1 minute. The sonicated supports were then coated with 500 nm Stöber silica particles by manual rubbing of dry Stöber silica powder with a gloved finger covered by Teflon tape. The supports were then dried at 70 °C for 4 hours, and heat treated at 1100 °C for 3 hours, with heating and cooling rates of 2 °C/min and 4 °C/min, respectively. This rubbing-sintering process was repeated 5-6 times until the quartz fibers were no longer visible by SEM. The 500 nm Stöber silica-coated supports were then coated with 50 nm Stöber silica particles through a similar rubbing process. 50 nm Stöber silica rubbing was only done once, and the coated supports were sintered at 400 °C for 4 hours, with heating and cooling rates of 2 °C/min and 4 °C/min. The Stöber silica-coated supports were coated with the previously synthesized suspension of MFI nanosheets in octanol through vacuum filtration. The concentration of nanosheet suspension was adjusted in order to result in ~75-100 nm-thick nanosheet coating. Following the coating, the supports were dried at 150°C for 6 hours and calcined at 400 °C for 6 hours, with heating and cooling rates of 1 °C/min. This nanosheet coating process was repeated once more in order to achieve a final seed layer thickness of 150-200 nm. Secondary growth of nanosheets was then carried out using the gel-less method. ⁴ The coated supports were soaked in 0.025M TPAOH solution for 5 minutes. Secondary growth was carried out by placing the presoaked membrane in a sealed autoclave and heating at 200°C for 24 hours. The secondary-grown membranes were then calcined at 550°C for 8 hours with heating and cooling ramp rates of 0.5°C/min under 150 sccm air flow.

4. Xylene isomer separation measurements. Low temperature and low partial pressure xylene separation was carried out by sealing the membrane in a stainless-steel cell and flowing the gases

in Wicke-Kallenbach mode.^{4,5} G75H Perlast perfluoroelastomer (Precision Polymer Engineering Ltd.) o-rings (rated to 320 °C) were used for membrane sealing. The membrane cell consisted of a plugged 1" VCR fitting (Swagelok®) which was modified by making holes on the top VRC gland for feed and retentate lines, and bottom VCR gland for sweep and permeate lines. The top surfaces of the glands were recessed in order to accommodate the membrane and o-rings. The membrane was sandwiched between the o-rings and placed in the cell. A torque of 60 N-m was applied through the use of a torque wrench, which was sufficient to form a gas tight seal.

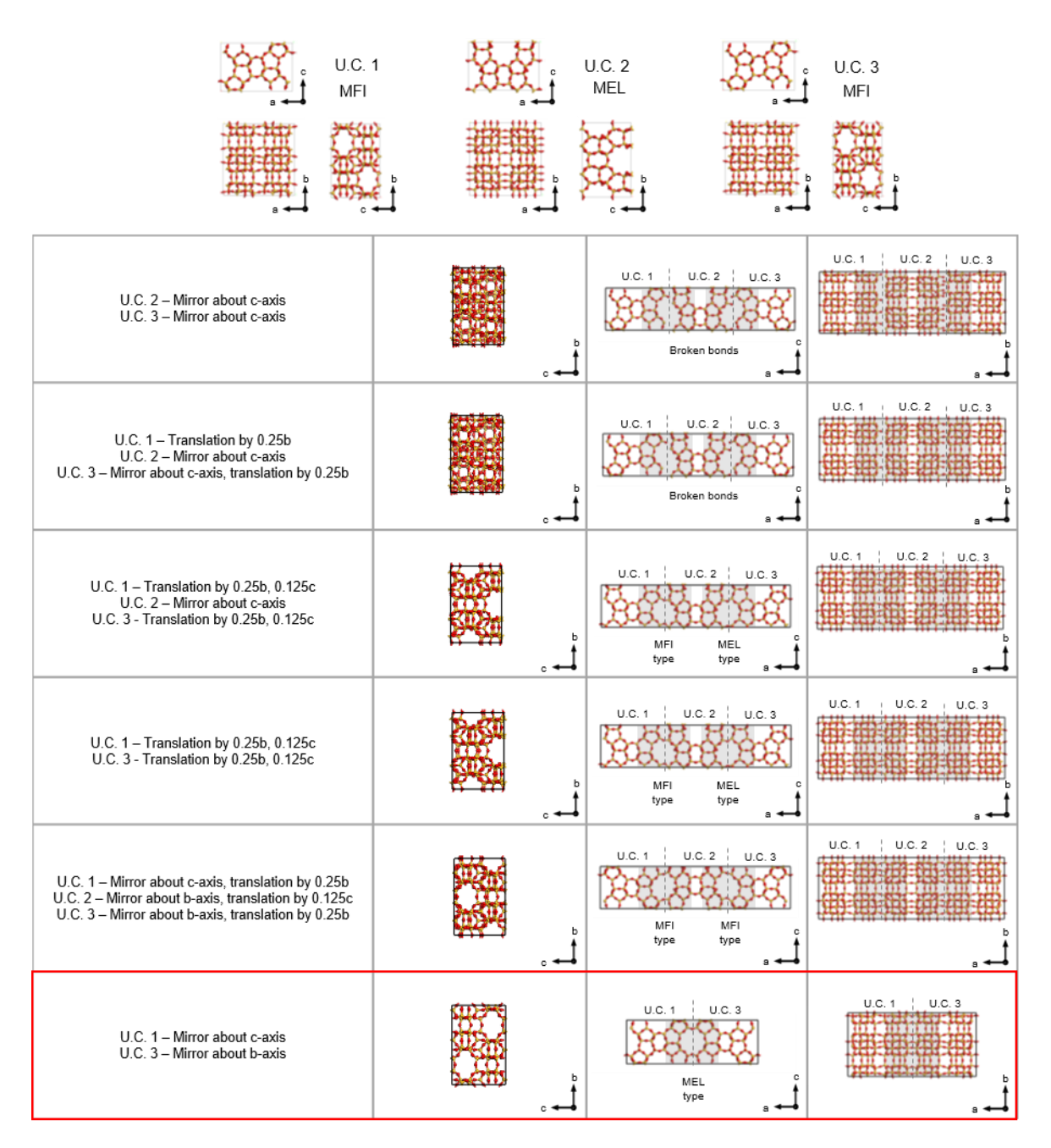
The total pressures of feed and permeate were maintained at atmospheric pressure. The xylene feed stream was generated by bubbling a 70 sccm flow of helium through a liquid xylene mixture in a glass bubbler heated using a water jacket. All lines following the bubbler were heated using heating tapes to prevent xylene condensation. The membrane cell was placed in a convection oven to maintain a uniform temperature (typically 150 °C). The back of the membrane was swept with a 20 sccm Helium sweep stream. The composition of permeate as well as feed was determined using a gas chromatograph (GC, Agilent, 7890B).

Membranes which had been previously tested under Wicke-Kallenbach mode were transferred to the high temperature, high pressure xylene separation system without removal of membrane from the cell. Liquid feed (47.5% p-xylene, 47.5% o-xylene and 5% trimethyl benzene) was fed using a syringe pump (ISCO, model number 500D) at a constant flow rate (0.1 mL/min). The feed pressure was varied through the syringe pump. The feed was passed through a preheater, which vaporized it, prior to being fed to the membrane. The membrane cell was maintained at a temperature between 275-300 °C. The permeate side was maintained under vacuum (~9-12 kPa permeate side pressure) to increase the driving force for diffusion. In addition, a helium sweep stream could also be used. The retentate and permeate compositions were determined through

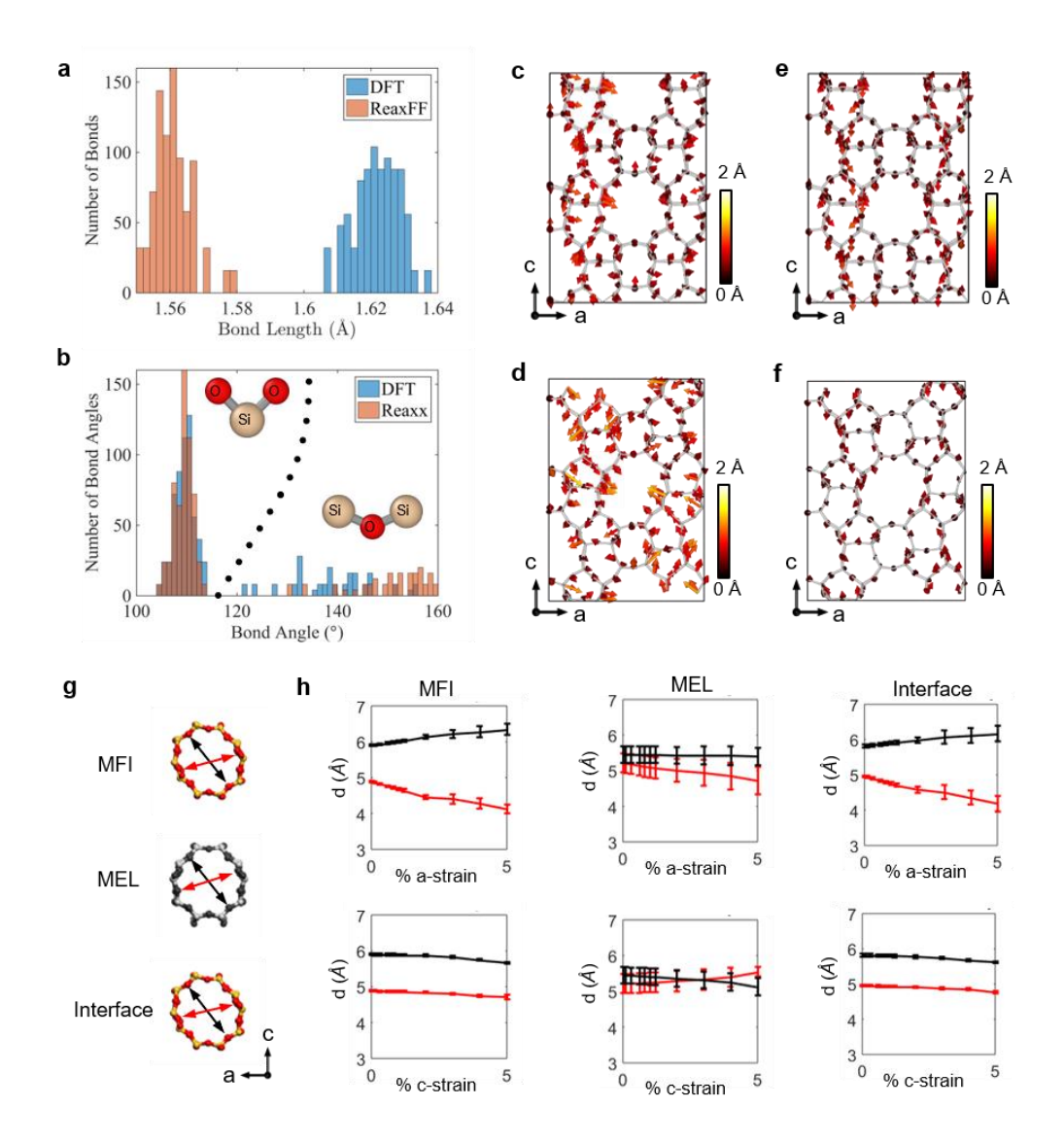
online GC sampling. The flux was determined by weighing the condensed permeate after a known period of time.

- 5. Direct synthesis of MEL-containing MFI nanosheets in the presence of graphite. C22-6-6Br2 structure directing agent (SDA) was prepared by a synthesis procedure reported in the literature.¹ **Synthesis** carried composition of was out at the gel 100SiO₂:7.5SDA:10NaOH:36Na₂SO₄:4000H₂O. First, 0.12 g NaOH and 1.5336 g Na₂SO₄ were dissolved in 6.6 g DI water (Base solution). 1.635 g C₂₂₋₆₋₆Br₂ was dissolved in 15 g DI water at 70 °C (structure directing agent (SDA) solution). The base solution was added to cool SDA solution with stirring and then 6.25 g tetraethyl orthosilicate (TEOS) was added to the solution at room temperature. The solution was placed into an oil bath preheated at 60 °C for 6 h with stirring. The resultant gel was mixed with desired amounts of graphite power (FP 99.95% pure, Graphit Kropfmühl AG) by hand-shaking and stirred for 10 min. The mixture was transferred into a Teflonliner of stainless-steel autoclave. To the gel obtained, 100mg of graphite power (FP 99.95% pure, Graphit Kropfmühl AG) was added and mixed by hand-shaking followed by stirring for 10 min. The hydrothermal treatment was carried out at 180 °C for 2 days under static condition and then additional 18 days under rotation (60 r/min). The obtained solid was diluted in DI water and centrifuged at 11,000 rpm for 20 min. Washing with DI water was repeated until the pH of the solution became 9.
- **6. De-lamination of MEL-containing MFI nanosheets by melt-compounding.** 1 g of the obtained solid was mixed with 14 g of oligomeric polystyrene (PS) (Eastman Chemical Company, PiccolasticTM A75 hydrocarbon resin, Mw~1,300 g/mol, Tg~35 °C) and added into a melt-compounder (Xplore® micro compounder MC15) and mixed for 1 h at 250 rpm at 90 °C.^{2,3} 15 g of the extruded nanocomposite material was dissolved in 100 mL of toluene and then centrifuged

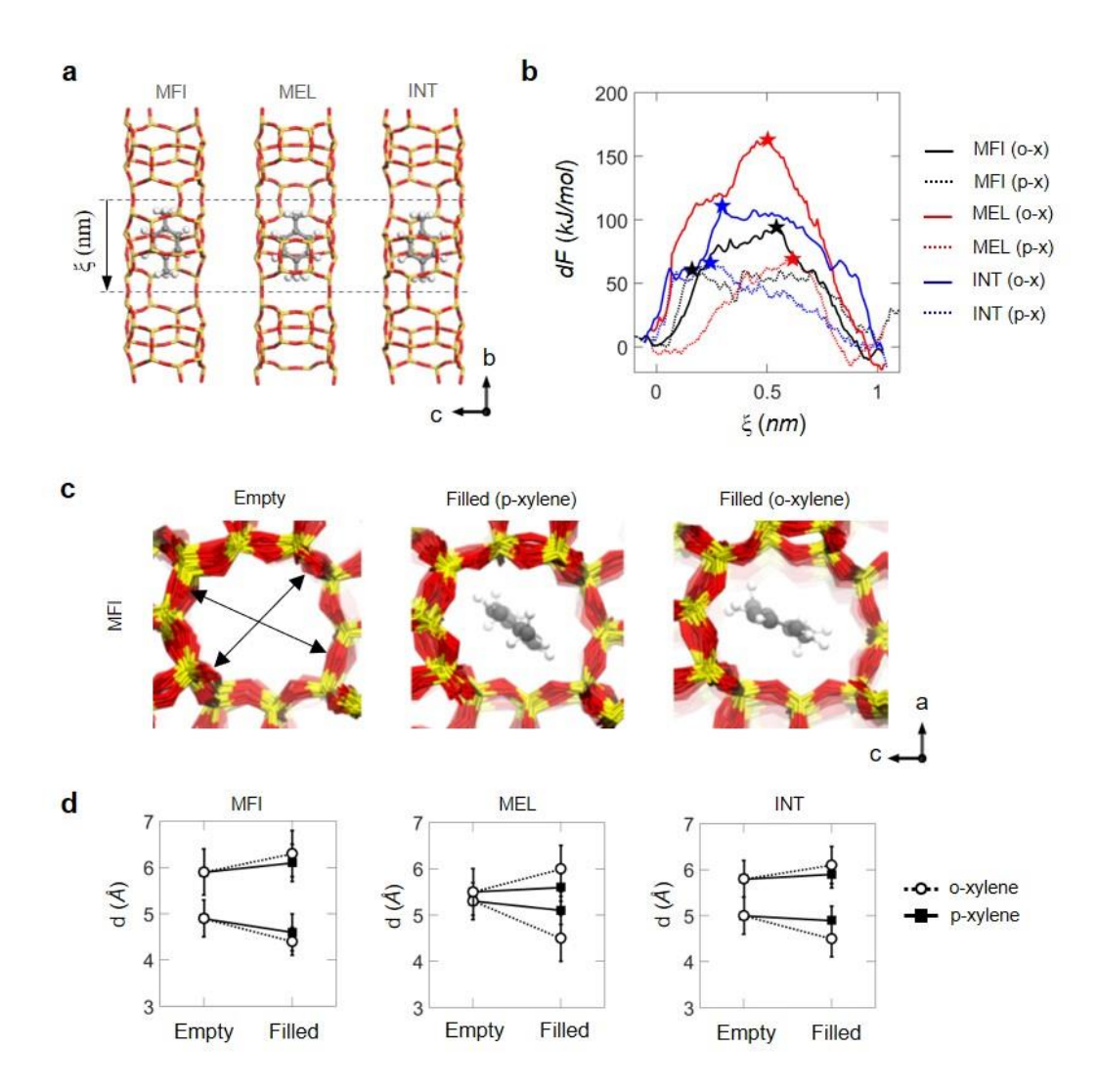
at 40,000 g for 20 min. The nanosheets at the bottom of the centrifuge tube were washed three times with fresh toluene to remove the residual PS. The purified delaminated nanosheets were redispersed in ethanol and dried at 70 °C.



Supplementary Figure 1. Examples of different symmetry operations (mirror & translation) between MFI and MEL unit cells. Resulting heterostructures are shown above along three different projections. Structures are periodic in a-, b- and c-direction. Interfaces (highlighted in gray) show loss in atomic connectivity, MFI type or MEL type structure depending on the symmetry operations involved during creation of the heterostructure. Boxed in red (at the bottom row) is the structure used for first-principle simulations of diffusivity ratios of p-/o-xylene. This structure was chosen since it has the minimum number of atoms fully connected to form MFI, MEL, and Interfacial pores, thereby making the simulations computationally efficient.

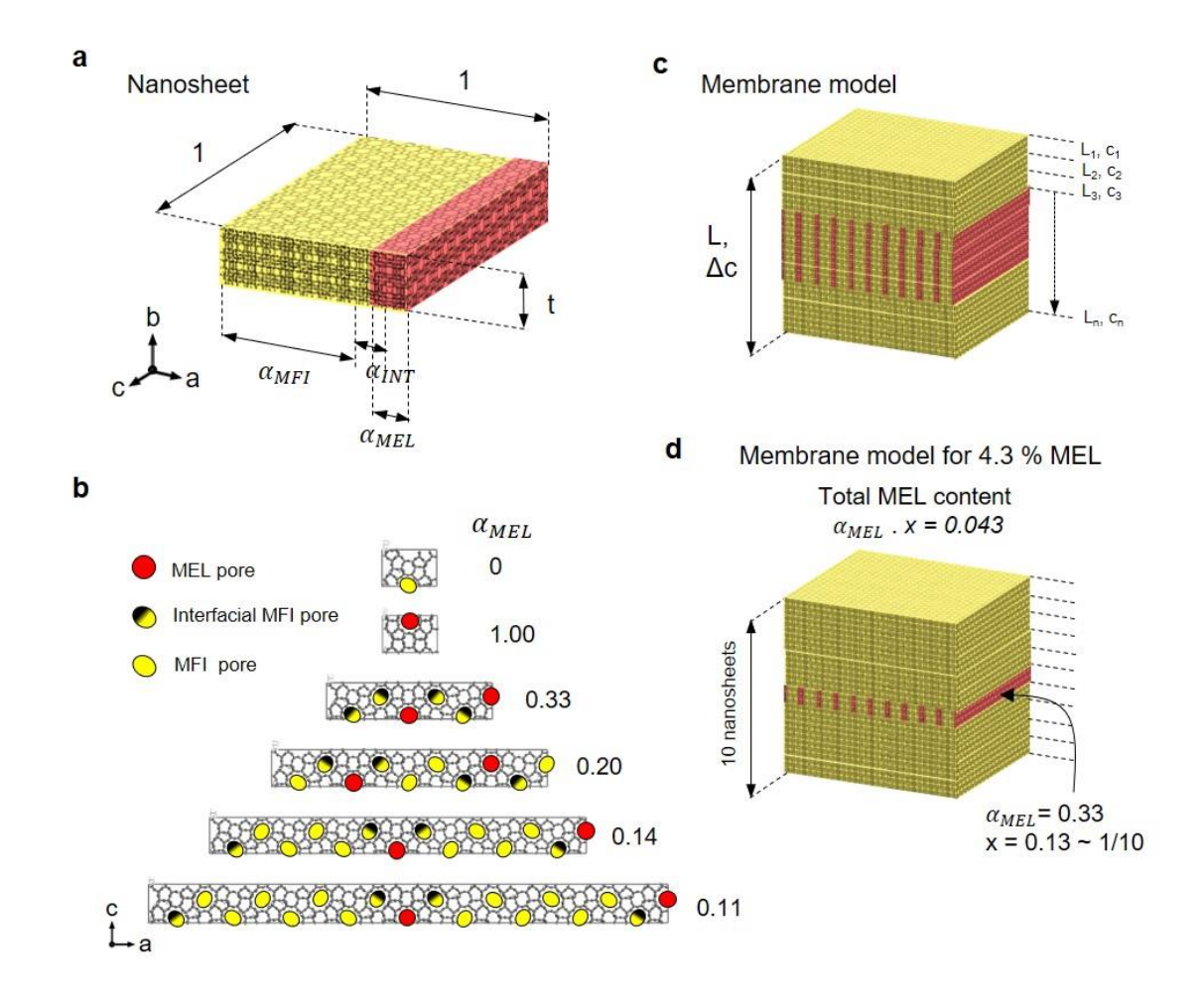


Supplementary Figure 2. Simulated response to compressive strain for MFI and MFI-MEL structure. Histograms comparing the **a**, the bond lengths and **b**, bond angles measured from the MFI model, relaxed using DFT and ReaxFF potentials. ReaxFF relaxed atomic structure models are shown along with colored arrows indicating the direction of motion for atoms upon 1% compression strain along a-direction for **c**, MEL structure, **d**, MFI structure and upon compression along c-direction for **e**, MEL structure and **f**, MFI structure. Colors of the arrow indicate the distance moved according to the color-bar shown. **g**, MFI, MEL, and interface pores shown in main text Fig. 4. **h**, Distances along the marked arrows in g, are plotted for MFI, MEL and interfacial pore with respect to applied strain. Error bars are calculated as the standard deviation of six measurements of distances along the **b**-direction.

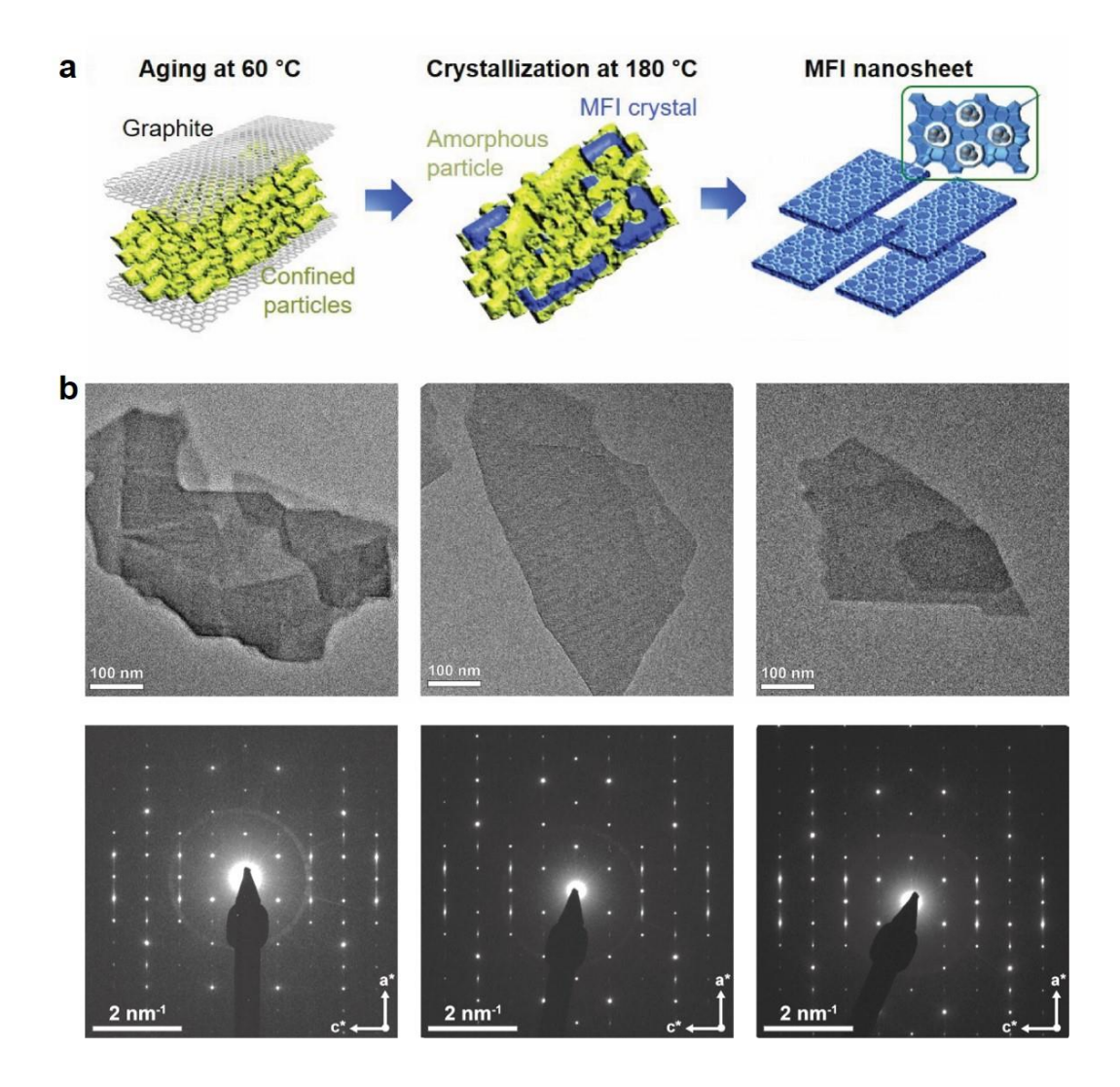


Supplementary Figure 3. Diffusivity of p-xylene and o-xylene molecule through the pores. a, a-axis projection of MFI, MEL and Interfacial (INT) pore with p-xylene molecule at the center. b, Free energy barrier for p-xylene and o-xylene molecule passing through the narrowest region along the b-axis (highlighted by the dotted lines in panel a) of MEL, MFI and interfacial pores. Assuming the same pre-exponential factor for diffusion of o-xylene and p-xylene at 573 K, we estimate p-xylene/o-xylene diffusivity ratios of 1.1x10³ in MFI, 3.6x10⁵ in MEL, and 1.2x10⁴ in the MFI-MEL interfacial channel. c, 20 snapshots of the MFI atomic structure are overlaid using the VMD software, when MFI pore is empty, contains p-xylene and o-xylene at the location represented by ★ markers in panel b. d, Changes in pore size measured along the marked directions in panel c when MFI, MEL and interface pores are occupied by o-xylene and p-xylene molecules. Distances between oxygen atoms are plotted after subtracting 2.7 Å to account for the van der Waals diameter of an oxygen atom. The error bars represent standard deviations in distance measurements during the trajectories.

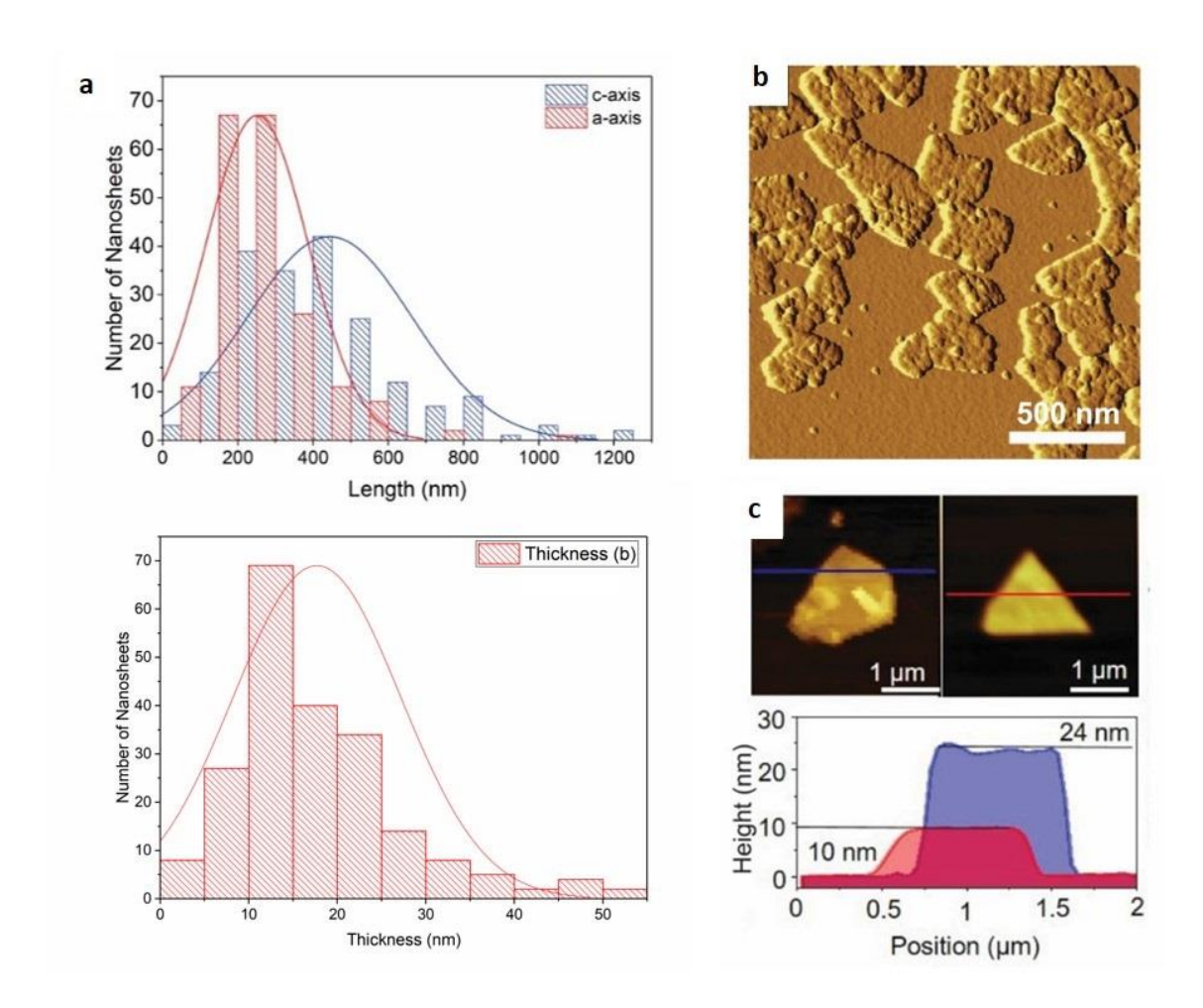
Note: Since the curvature for o-xylene in MEL at the barrier is by far larger than for any other case, the corresponding pre-exponential factor is likely to be larger than the rest and the p-x/o-x selectivity in MEL is likely overestimated.



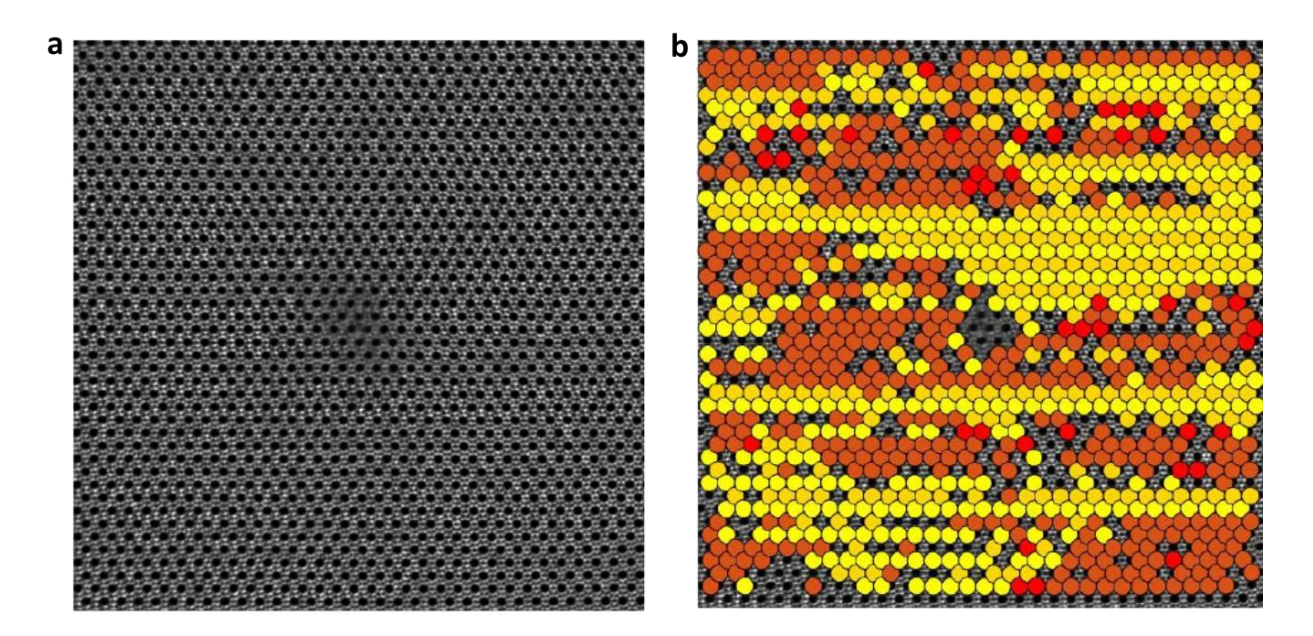
Supplementary Figure 4. MFI-MEL heterostructures and simplified membrane model. a, Model Nanosheet heterostructure formed by connecting MFI unit cells with MEL unit cell, resulting in interfacial (INT) pores. The fraction of MFI, MEL and INT is depicted as α_{MFI} , α_{MEL} , α_{INT} , respectively for a nanosheet with unit length along **a-** and **c-** direction and thickness t along **b-**direction. **b,** Periodic structures along **a-** and **c-**direction used for calculating the young's modulus and estimating the nanosheet selectivities reported in the main text. All structures were 1.5 u.c. thick along **b-**direction and were relaxed using ReaxFF potentials. **c,** Model of a membrane with thickness L consisting of n nanosheets stacked over each other and having a loading difference of Δc along b-direction for p-xylene and o-xylene. **d,** Membrane model showing a possible distribution of MEL in a membrane containing 4.3% MEL which results in 5.5-fold improvement in selectivity as compared to a pure MFI membrane.



Supplementary Figure 5. TEM examination of high-MEL-content nanosheets made under graphitic confinement. a, Schematic for the growth of MEL-containing nanosheets prepared using $C_{22-6-6}Br_2$ SDA under graphitic confinement. b, BF-TEM images of the nanosheets (top) and the corresponding SAED pattern (bottom). The diffraction spots (h+l=odd) show streaking along a^* direction for these nanosheets indicating the presence of MEL.



Supplementary Figure 6. Length, width and thickness measurements of high-MEL-content nanosheets made under graphitic confinement. Histogram of measured lengths along **a-, b-** and **c-**direction from ADF-STEM images for MEL-containing nanosheets prepared through graphitic confinement (a-direction: 250+/-140 nm, b-direction: 18+/-9, c-direction: 440+/-220 nm). **b,** AFM image of MEL-containing nanosheets and **c,** linescans (red and blue) across individual MEL-containing nanosheets show thickness of 10 nm and 24 nm.



Supplementary Figure 7. High-MEL-content nanosheets made under graphitic confinement. a, Filtered ADF-STEM image. **b,** same ADF-STEM image with colored circles for MFI (yellow) and MEL (red) unit cells that are identified using the template matching algorithm described in detail in methods and Extended Data Fig. 4.

Table S1: Young's Modulus (E) for nanosheets with different MEL fractions (α_{MEL})

α_{MFI}	α_{MEL}	$lpha_{INT}$	<i>E</i> (a , GPa)	$E\left(\mathbf{c},\mathrm{GPa}\right)$
0.00	1.00	0.00	63.1	55.3
0.00	0.33	0.67	57.2	55.7
0.40	0.20	0.40	55.3	56.3
0.57	0.14	0.29	54.6	56.5
0.67	0.11	0.22	54.3	56.6
1.00	0.00	0.00	53.6	57.5

Table S2: Selectivity of nanosheets (*NS*) with different 1-D-MEL fractions (α_{MEL}) using Equation 1 for T=573K.

α_{MFI}	α_{MEL}	α_{INT}	R^o	R^p	$NS/[A^p/A^o]$
0.00	1.00	0.00	1.9E+06	5.7	3.6E+08
0.00	0.75	0.25	1.4E+02	4.7	32,000
0.00	0.50	0.50	6.8E+01	4.0	18,000
0.00	0.33	0.67	50.7	3.7	15,000
0.20	0.27	0.53	4.6	2.4	2,100
0.40	0.20	0.40	2.4	1.8	1,500
0.57	0.14	0.29	1.7	1.5	1,300
0.67	0.11	0.22	1.5	1.3	1,200
1.00	0.00	0.00	1.0	1.0	1,100

Note: At 573K the diffusivity ratios needed to calculate R^p and R^o are:

 $\frac{D_{MFI}^p}{D_{MEL}^p} = 5.7$; $\frac{D_{MFI}^p}{D_{INT}^p} = 3.1$; $\frac{D_{MFI}^o}{D_{MEL}^o} = 1,900,000$; $\frac{D_{MFI}^o}{D_{INT}^o} = 34$. These ratios are calculated assuming that the pre-exponential factors depend only on the component and do not depend on framework type MFI, INT or MEL. As noted in Supplementary Fig. 3, since the curvature for o-xylene in MEL at the barrier is by far larger than for any other case, the corresponding pre-exponential factor is likely to be larger than the rest and the $\frac{D_{MFI}^o}{D_{MEL}^o} = 1,900,000$ is an overestimation.

Table S3: Selectivity enhancement (MS'/MS from Eq. 2) due to 1-D-MEL.

fraction of MEL containing nanosheets	Membrane selectivity enhancement (MS'/MS)					
(x)	$\alpha_{MEL} = 0.11$	$\alpha_{MEL} = 0.20$	$\alpha_{MEL} = 0.27$	$\alpha_{MEL} = 0.33$		
0	1.0	1.0	1.0	1.0		
0.1	1.0 1.1 1.2		1.2	4.7		
0.13	-	-	-	5.5		
0.16	-	-	1.3	-		
0.2	1.0	1.1	1.4	7.1		
0.3	1.1	1.1	1.5	8.8		
0.4	1.1	1.2	1.6	10.0		
0.5	1.1	1.2	1.7	11.0		
0.6	1.1	1.2	1.7	11.8		
0.7	1.1	1.3	1.8	12.4		
0.8	1.1	1.3	1.8	12.9		
0.9	1.1	1.3	1.9	13.3		
1.0	1.2	1.3	1.9	13.7		

 α_{MEL} is the fraction of MEL within the nanosheets. x is the fraction of MEL-containing nanosheets that form the membrane. Total MEL content of the membrane is the product ($\alpha_{MEL}.x$). Two cases for total MEL content of 4.3% (or 0.043) in the membrane are highlighted in grey.

References

- 1. Choi, M. *et al.* Stable single-unit-cell nanosheets of zeolite MFI as active and long-lived catalysts. *Nature* **461**, 246–9 (2009).
- 2. Varoon, K. *et al.* Dispersible exfoliated zeolite nanosheets and their application as a selective membrane. *Science* **334**, 72–5 (2011).
- 3. Zhang, H. *et al.* Open-Pore Two-Dimensional MFI Zeolite Nanosheets for the Fabrication of Hydrocarbon-Isomer-Selective Membranes on Porous Polymer Supports. *Angew. Chemie Int. Ed.* **55**, 7184–7187 (2016).
- 4. Agrawal, K. V. *et al.* Oriented MFI Membranes by Gel-Less Secondary Growth of Sub-100 nm MFI-Nanosheet Seed Layers. *Adv. Mater.* **27**, 3243–9 (2015).
- 5. Jeon, M. Y. *et al.* Ultra-selective high-flux membranes from directly synthesized zeolite nanosheets. *Nature* **543**, 690 (2017).